

LhARA: The Laser-hybrid Accelerator for Radiobiological Applications

G. Aymar¹, T. Becker², S. Boogert³, M. Borghesi⁴, R. Bingham^{5,1},
C. Brenner¹, P. Burrows⁶, O.C. Ettliger⁷, T. Dascalu⁷, S. Gibson³,
T. Greenshaw⁸, S. Gruber⁹, D. Gujral¹⁰, C. Hardiman¹⁰, J. Hughes⁸,
W.G. Jones^{7,19}, K. Kirkby¹¹, A. Kurup⁷, J-B. Lagrange¹, K. Long^{7,1}, W. Luk⁷,
J. Matheson¹, P. Mckenna⁵, R. Mclauchlan¹⁰, Z. Najmudin⁷, H.T. Lau⁷,
J.L. Parsons^{8,20}, J. Pasternak^{7,1}, J. Pozimski^{7,1}, K. Prise⁴, M. Puchalska¹²,
P. Ratoff¹³, G. Schettino^{14,18}, W. Shields³, S. Smith¹⁵, J. Thomason¹,
S. Towe¹⁶, P. Weightman⁸, C. Whyte⁵, R. Xiao¹⁷

¹ STFC Rutherford Appleton Laboratory, Harwell Oxford, Didcot, OX11 0QX, UK

² Maxeler technologies Limited, 3 Hammersmith Grove, London W6 0ND, UK

³ Royal Holloway, University of London, Egham, Surrey, TW20 0EX, UK

⁴ Queens University Belfast, University Road, Belfast, BT7 1NN, Northern Ireland, UK

⁵ University of Strathclyde, 16 Richmond Street, Glasgow, G1 1XQ, UK

⁶ The John Adams Institute, Denys Wilkinson Building, Keble Road, Oxford OX1 3RH, UK

⁷ Imperial College London, Exhibition Road, London, SW7 2AZ, UK

⁸ University of Liverpool, Liverpool L3 9TA, UK

⁹ Christian Doppler Laboratory for Medical Radiation Research for Radiation Oncology, Medical University of Vienna, Spitalgasse 23, 1090 Vienna, Austria

¹⁰ Imperial College NHS Healthcare Trust, The Bays, South Wharf Road, St Mary's Hospital, London W2 1NY, UK

¹¹ University of Manchester, Oxford Road, Manchester, M13 9PL, UK

¹² Technische Universität Wien, Atomintitut, Stadionallee 2, 1020 Vienna, Austria

¹³ The Cockcroft Institute Daresbury Laboratory, Sci-Tech Daresbury, Daresbury, Warrington, WA4 4AD, UK

¹⁴ National Physical Laboratory, Hampton Road, Teddington, Middlesex, TW11 0LW, UK

¹⁵ STFC Daresbury Laboratory, Daresbury, Cheshire, WA4 4AD, UK

¹⁶ Leo Cancer Care, Broadview, Windmill Hill, Hailsham, East Sussex, BN27 4RY, UK

¹⁷ Cororain, 14F, Changfu Jinmao Building (CFC), Trade-free Zone, Futian District, Shenzhen, Guangdong, China

¹⁸ University of Surrey, 388 Stag Hill, Guilford, GU2 7XH, UK

¹⁹ Imperial Patient and Public Involvement Group (IPPIG), Imperial College London, Exhibition Road, London, SW7 2AZ, UK

²⁰ The Clatterbridge Cancer Centre, Bebington, CH63 4JY, UK

Correspondence*:

A. Kurup

a.kurup@imperial.ac.uk

2 ABSTRACT

3 The ‘Laser-hybrid Accelerator for Radiobiological Applications’, LhARA, is conceived as a novel,
4 uniquely-flexible facility dedicated to the study of radiobiology. The technologies demonstrated
5 in LhARA, which have wide application, will be developed to allow particle-beam therapy to be
6 delivered in a completely new regime, combining a variety of ion species in a single treatment
7 fraction and exploiting ultra-high dose rates. LhARA will be a hybrid accelerator system in which
8 laser interactions drive the creation of a large flux of protons or light ions that are captured using
9 a plasma (Gabor) lens and formed into a beam. The laser-driven source allows protons and ions
10 to be captured at energies significantly above those that pertain in conventional facilities, thus
11 evading the current space-charge limit on the instantaneous dose rate that can be delivered.
12 The laser-hybrid approach, therefore, will allow the vast “terra incognita” of the radiobiology that
13 determines the response of tissue to ionising radiation to be studied with protons and light
14 ions using a wide variety of time structures, spectral distributions, and spatial configurations at
15 instantaneous dose rates up to and significantly beyond the ultra-high dose-rate ‘FLASH’ regime.

16 It is proposed that LhARA be developed in two stages. In the first stage, a programme of *in*
17 *vitro* radiobiology will be served with proton beams with energies between 10 MeV and 15 MeV.
18 In stage two, the beam will be accelerated using a fixed-field accelerator (FFA). This will allow
19 experiments to be carried out *in vitro* and *in vivo* with proton beam energies of up to 127 MeV.
20 In addition, ion beams with energies up to 33.4 MeV per nucleon will be available for *in vitro*
21 and *in vivo* experiments. This paper presents the conceptual design for LhARA and the R&D
22 programme by which the LhARA consortium seeks to establish the facility.

23 LAY SUMMARY

24 It is well established that radiation therapy (RT) is an effective treatment for many types of cancer.
25 Most treatments are delivered by machines that accelerate electrons which are then used to
26 produce a beam of high-energy photons (X-rays) which are directed at a tumour to kill cancer
27 cells. However, healthy tissue anywhere in the path of the photon beam is also irradiated and so
28 can be damaged. Modern X-ray therapy is able to reduce this damage by using several beams at
29 different angles.

30 Recent years have seen the use of a new type of machine in which protons are accelerated to
31 produce proton beams (rather than photon beams) which are directed at a tumour. These proton
32 beams can be arranged to deposit almost all of their energy in a small volume within a tumour so
33 they cause little damage to healthy tissue; a major advantage over photon beams. But proton
34 machines are large and expensive, so there is a need for the development of proton machines
35 that are smaller, cheaper and more flexible in how they can be used.

36 The LhARA project is aimed at the development of such proton machines using a new approach
37 based on high powered lasers. Such new machines could also make it easier to deliver the dose
38 in very short high-intensity pulses and as a group of micro-beams—exciting recent research has
39 shown that this brings improved effectiveness in killing cancer cells while sparing healthy tissue.
40 The technology to be proved in LhARA should enable a course of RT to be delivered in days
41 rather than weeks and should be more effective.

42 Scientifically, there is a need to understand much better the basic processes by which radiation
43 interacts with biological matter to kill cancer cells—the investigation of these processes involves
44 physics as well as biology. Thus the most important aim of LhARA is to pursue this radiobiological

45 research in new regimes and from this to develop better treatments. LhARA will also pursue
46 technological research into laser-hybrid accelerators.

47 **Keywords:** Radiobiology, Novel acceleration, Proton beam therapy, Ion beam therapy, Laser-driven acceleration, Plasma lens, Fixed
48 field alternating gradient acceleration

1 INTRODUCTION

49 Cancer is the second most common cause of death globally [The World Health Organisation (2020)]. In
50 2018, 18.1 million new cancer cases were diagnosed, 9.6 million people died of cancer-related disease, and
51 43.8 million people were living with cancer [Bray et al. (2018); Fitzmaurice et al. (2018)]. It is estimated
52 that 26.9 million life-years could be saved in low- and middle-income countries if radiotherapy capacity
53 could be scaled up [Atun et al. (2015)]. Novel techniques incorporated in facilities that are at once robust,
54 automated, efficient, and cost-effective are required to deliver the required scale-up in provision.

55 Radiation therapy (RT), a cornerstone of cancer treatment, is used in over 50% of cancer patients [Datta
56 et al. (2019)]. The most frequently used types of radiotherapy employ photon or electron beams with
57 MeV-scale energies. Proton and ion beams offer substantial advantages over X-rays because the bulk
58 of the beam energy is deposited in the Bragg peak. This allows dose to be conformed to the tumour
59 while sparing healthy tissue and organs at risk. The benefits of proton and ion-beam therapy (PBT) are
60 widely recognised. PBT today is routinely delivered in fractions of ~ 2 Gy per day over several weeks;
61 each fraction being delivered at a rate of $\lesssim 10$ Gy/minute deposited uniformly over the target treatment
62 volume. Exciting evidence of therapeutic benefit has recently been reported when dose is delivered at
63 ultra-high dose-rate, $\gtrsim 40$ Gy/s (“FLASH” RT) [Favaudon et al. (2014); Vozenin et al. (2019)], or provided
64 in multiple micro-beams with diameter less than 1 mm distributed over a grid with inter-beam spacing of
65 ~ 3 mm [Prezado et al. (2017)]. However, the radiobiological mechanisms by which the therapeutic benefit
66 is generated are not entirely understood.

67 LhARA, the Laser-hybrid Accelerator for Radiobiological Applications, is conceived as the new, highly
68 flexible, source of radiation that is required to explore the vast “terra incognita” of the mechanisms by
69 which the biological response to ionising radiation is determined by the physical characteristics of the beam.
70 A high-power pulsed laser will be used to drive the creation of a large flux of protons or light ions which
71 are captured and formed into a beam by strong-focusing plasma lenses. The laser-driven source allows
72 protons and ions to be captured at energies significantly above those that pertain in conventional facilities,
73 thus evading the current space-charge limit on the instantaneous dose rate that can be delivered. The plasma
74 (Gabor) lenses provide the same focusing strength as high-field solenoids at a fraction of the cost. Rapid
75 acceleration will be performed using a fixed-field alternating-gradient accelerator (FFA) thereby preserving
76 the unique flexibility in the time, energy, and spatial structure of the beam afforded by the laser-driven
77 source.

78 We propose that LhARA be developed in two stages. In the first stage, the laser-driven beam, captured
79 and transported using plasma lenses and bending magnets, will serve a programme of *in vitro* radiobiology
80 with proton beams of energy of up to 15 MeV. In stage two, the beam will be accelerated using an FFA. This
81 will allow experiments to be carried out *in vitro* and *in vivo* with proton-beam energies of up to 127 MeV.
82 Ion beams (including C^{6+}) with energies up to 33.4 MeV per nucleon will also be available.

83 The laser pulse that initiates the production of protons or ions at LhARA may be triggered at a repetition
84 rate of up to 10 Hz. The time structure of the beam may therefore be varied to interrupt the chemical
85 and biological pathways that determine the biological response to ionising radiation with 10 ns to 40 ns
86 long proton or ion bunches repeated at intervals as small as 100 ms. The technologies chosen to capture,
87 transport, and accelerate the beam in LhARA have been made so that this unique capability is preserved.
88 The LhARA beam may be used to deliver an almost uniform dose distribution over a circular area with
89 a maximum diameter of between 1 cm and 3 cm. Alternatively the beam can be focused to a spot with
90 diameter of ~ 1 mm.

91 The technologies demonstrated in LhARA have the potential to be developed to make “best in class”
92 treatments available to the many. The laser-hybrid approach will allow radiobiological studies and eventually
93 radiotherapy to be carried out in completely new regimes, delivering a variety of ion species in a broad
94 range of time structures, spectral distributions, and spatial configurations at instantaneous dose rates up to
95 and potentially significantly beyond the current ultra-high dose-rate “FLASH” regime.

96 The LhARA consortium is the multidisciplinary collaboration of clinical oncologists, medical and
97 academic physicists, biologists, engineers, and industrialists required to deliver such a transformative
98 particle-beam system. With its “pre Conceptual Design Report” (pre-CDR) [The LhARA consortium
99 (2020)] the consortium lays out its concept for LhARA, its potential to serve a ground-breaking programme
100 of radiobiology, and the technological advances that will be made in its execution. The work presented in
101 the LhARA pre-CDR lays the foundations for the development of full conceptual and technical designs
102 for the facility. The pre-CDR also contains a description of the R&D that is required to demonstrate the
103 feasibility of critical components and systems. This paper presents a summary of the contents of the
104 pre-CDR and lays out the vision of the consortium.

105

2 MOTIVATION

106 Conventional (X-ray) RT is one of the most effective cancer treatments, particularly for solid tumours
107 including head and neck tumours and glioblastoma. The dose delivered using X-rays falls approximately
108 exponentially with depth; this characteristic implies a fundamental limit on the maximum dose that can
109 be delivered to the tumour without delivering an unacceptably large dose to healthy tissue. For a given
110 treatment beam-entry point, tumours that lie deep within the patient will receive a dose significantly lower
111 than that delivered to the healthy tissues through which the beam passes on its way to the treatment site.
112 X-rays that pass through the tumour will also deliver a dose to the tissues that lie behind. Dose delivered to
113 healthy tissues can cause the death of the healthy cells and create adverse side effects. Furthermore, the
114 maximum X-ray dose that can be delivered is limited by the presence of sensitive organs such as the brain
115 and spinal cord. This situation is particularly acute in infants for whom dose to healthy tissue, sensitive
116 organs, and bone can lead to developmental issues and a higher probability of secondary malignancies later
117 in life.

118 RT delivered using protons and ions, particle-beam therapy (PBT), has the potential to overcome some of
119 the fundamental limitation of X-rays in cancer treatment [Loeffler and Durante (2013)]. The physics of
120 the interaction between ionising radiation and tissue determines the radiobiological effect. Energy loss
121 through ionisation is the dominant mechanism at the beam energies relevant to PBT. The energy lost per
122 unit distance travelled, the linear energy transfer (LET), increases as the protons or ions slow down. At
123 low velocity, the rate of increase in LET is extremely rapid. This generates a ‘Bragg peak’ in the energy
124 deposited at the maximum range of the beam just as the protons or ions come to rest. In contrast to photons,
125 this characteristic allows the dose delivered to healthy tissue behind the Bragg peak to be reduced to zero for
126 protons, and almost to zero for carbon ions. Scanning the Bragg peak over the tumour volume enables an
127 increase in dose to the tumour while, in comparison to X-ray therapy, sparing tissues in front of the tumour.
128 By choosing carefully the treatment fields, dose to sensitive organs can be reduced significantly compared to
129 an equivalent treatment with photons, thus improving patient outcomes. The Particle Therapy Co-Operative
130 Group (PTCOG) currently lists 90 proton therapy facilities and 12 carbon ion therapy facilities. These
131 facilities are located predominantly in high-income countries [PTCOG (2020)]. Low- and middle-income
132 countries (LMIC) are relatively poorly served, indeed nearly 70% of cancer patients globally do not have
133 access to RT [Datta et al. (2019)]. Novel RT techniques incorporated in facilities that are robust, automated,

134 efficient, and cost-effective are therefore required to deliver the necessary scale-up in provision. This
135 presents both a challenge and an opportunity; developing the necessary techniques and scaling up RT
136 provision will require significant investment but will also create new markets, drive economic growth
137 through new skills and technologies and deliver impact through improvements in health and well-being.

138 **The case for a systematic study of the radiobiology of proton and ion beams**

139 The nature of the particle-tissue interaction confers on PBT the advantage that the dose can be precisely
140 controlled and closely conformed to the tumour volume. However, there are significant biological
141 uncertainties in the impact of ionising radiation on living tissue. The efficacy of proton and ion beams is
142 characterised by their relative biological effectiveness (RBE) in comparison to reference photon beams.
143 The treatment-planning software that is in use in the clinic today assumes an RBE value for protons of
144 1.1 [Paganetti and van Luijk (2013)]. This means that a lower dose of protons is needed to produce the
145 same therapeutic effect that would be obtained using X-rays. However, the rapid rise in the LET at the
146 Bragg peak leads to significant uncertainties in the RBE. It is known that RBE depends strongly on many
147 factors, including particle energy, dose, dose rate, the degree of hypoxia, and tissue type [Paganetti (2014)],
148 however, the radiobiology that determines these dependencies is not fully understood. A number of studies
149 have shown that there can be significant variation in RBE [Jones et al. (2018); Giovannini et al. (2016); Lühr
150 et al. (2018)]. Indeed, RBE values from 1.1 to over 3 have been derived from *in vitro* clonogenic-survival
151 assay data following proton irradiation of cultured cell lines derived from different tumours [Paganetti
152 (2014); Chaudhary et al. (2014); Wilkens and Oelfke (2004)]. Some of this variation may be due to the
153 positioning of the cells during irradiation relative to the Bragg peak. RBE values of ~ 3 are accepted for
154 high-LET carbon-ion irradiation, although higher values have been reported [Karger and Peschke (2017)].
155 RBE uncertainties for carbon and other ion species are at least as large as they are for protons.

156 Uncertainties in RBE can lead to an incorrect estimation of the dose required to treat a particular tumour.
157 Overestimation of the required dose leads to risk of damage to healthy tissue, while an underestimate can
158 lead to the tumour not being treated sufficiently for it to be eradicated. RT causes cell death by causing
159 irreparable damage to the cell's DNA. Hence, differences in RBE can also affect the spectrum of DNA
160 damage induced within tumour cells. Larger RBE values, corresponding to higher LET, can cause increases
161 in the frequency and complexity of DNA damage, particularly DNA double-strand breaks (DSB) and
162 complex DNA damage (CDD) where multiple DNA lesions are induced in close proximity [Vitti and
163 Parsons (2019); Carter et al. (2018)]. These DNA lesions are a major contributor to radiation-induced cell
164 death as they represent a significant barrier to the cellular DNA-repair machinery. Furthermore, the specific
165 nature of the DNA damage induced by ions determines the principal DNA-repair pathways employed
166 to effect repair; base excision repair is employed in response to DNA-base damage and single-strand
167 breaks, while non-homologous end-joining and homologous recombination is employed in response to
168 DSBs [Vitti and Parsons (2019)]. However, there are a number of other biological factors that contribute to
169 the efficacy of X-ray therapy and PBT, which produces greatly varying RBE in specific tumours, including
170 the intrinsic radiosensitivity of the tissue, the level of oxygenation (hypoxia), the growth and repopulation
171 characteristics, and the associated tumour micro-environment. Consequently, there is significant uncertainty
172 in the precise radiobiological mechanisms that arise and how these mechanisms are affected by PBT. A
173 more detailed and precise understanding is required for optimal patient-treatment strategies to be devised.
174 Detailed systematic studies of the biophysical effects of the interaction of protons and ions, under different
175 physical conditions, with different tissue types will provide important information on RBE variation and
176 could enable enhanced treatment-planning algorithms to be devised. In addition, studies examining the
177 impact of combination therapies with PBT (e.g. targeting the DNA damage response, hypoxia signalling
178 mechanisms and also the tumour micro-environment) are currently sparse; performing these studies will

179 therefore provide input vital to the development of future personalised patient-therapy strategies using PBT.
180 Such studies are needed, especially in the case of ion-beam radiotherapy.

181 **The case for novel beams for radiobiology**

182 PBT delivery to date has been restricted to a small number of beam characteristics. In a typical treatment
183 regimen the therapeutic dose is provided in a series of daily sessions delivered over a period of several
184 weeks. Each session consisting of a single fraction of ~ 2 Gy delivered at a rate of $\lesssim 5$ Gy/minute. The
185 dose in each fraction would be distributed uniformly over an area of several square centimetres. Recent
186 reports provide exciting evidence of therapeutic benefit when the dose is delivered at ultra-high dose
187 rate (> 40 Gy/s) “FLASH” RT [Favaudon et al. (2014); Vozenin et al. (2019)]. These studies indicate
188 significantly reduced lung fibrosis in mice, skin toxicity in mini-pigs, and reduced side-effects in cats with
189 nasal squamous-cell carcinoma. Varian has indicated that dose rates greater than 40 Gy/s are useful for
190 FLASH irradiation [Systems (2020)], while IBA have indicated that the FLASH phenomenon is observed at
191 dose rates above 33 Gy/s [IBA (2019)]. In addition, therapeutic benefit has been demonstrated with the use
192 of multiple micro-beams with diameter of less than 1 mm distributed over a grid with inter-beam spacing
193 of 3 mm [Prezado et al. (2017)]. However, there is still significant uncertainty regarding the thresholds
194 and the radiobiological mechanisms by which therapeutic benefit is generated in FLASH and micro-beam
195 therapy, which require extensive further study both *in vitro* and in appropriate *in vivo* models.

196 LhARA is designed to be a highly flexible source delivering the temporal, spectral, and spatial beam
197 structures that are required to elucidate the mechanisms by which the biological response to ionising
198 radiation is determined by the physical characteristics of the beam, including FLASH and micro-beam
199 effects. These comprehensive studies are not currently possible at clinical RT facilities. Thus the LhARA
200 facility will provide greater accessibility to stable ion beams, enable different temporal fractionation
201 schemes, and deliver reliable and reproducible biological data with fewer constraints than at current clinical
202 centres. The availability of several ion beams (from protons to heavier ions) within the same facility will
203 provide further flexibility and the ability to perform direct radiobiological comparisons of the effect of
204 different charged particles. In addition, LhARA will enable exhaustive evaluations of RBE using more
205 complex end-points (e.g. angiogenesis and inflammation) in addition to routine survival measurements. The
206 ability to evaluate charged particles in conjunction with other therapies (immunotherapy and chemotherapy),
207 and of performing *in vivo* experiments with the appropriate animal models is a huge advantage given
208 the current lack of evidence in these areas. LhARA therefore has the potential to yield the accumulation
209 of radiobiological data that can drive a significant change in current clinical practice. The simulations of
210 LhARA that are described in this document have been used to estimate the dose delivered as a function
211 of energy for protons and carbon ions. Details of the simulations can be found in sections 3.3 and 3.4.
212 The simulations show instantaneous particle rates on the order of 10^9 particles per shot can be achieved,
213 corresponding to average dose rates up to $\gtrsim 120$ Gy/s for protons and $\gtrsim 700$ Gy/s for carbon ions. These
214 estimates are based on the baseline specifications for LhARA.

215 **Laser-hybrid beams for radiobiology and clinical application**

216 High-power lasers have been proposed as an alternative to conventional proton and carbon-ion facilities
217 for radiotherapy [Bulanov et al. (2002); Fourkal et al. (2003); Malka et al. (2004)]. The capability of
218 laser-driven ion beams to generate protons and high-LET carbon ions at FLASH dose rates is a significant
219 step forward for the provision of local tumour control whilst sparing normal tissue. High-power lasers
220 have also been proposed to serve as the basis of electron, proton and ion-beams for radiobiology [Kraft
221 et al. (2010); Fiorini et al. (2011); Doria et al. (2012); Zeil et al. (2013); Masood et al. (2014); Zlobinskaya
222 et al. (2014)]. More recent projects (e.g. A-SAIL [A-SAIL Project (2020)], ELI [Cirrone et al. (2013)] and

223 SCAPA [Wiggins et al. (2019)] will also investigate radiobiological effects using laser-driven ion beams.
224 These studies will also address various technological issues [Manti et al. (2017); Romano et al. (2016);
225 Masood et al. (2017); Chaudhary et al. (2017); Margarone et al. (2018)].

226 The LhARA collaboration's concept is to exploit a laser to drive the creation of a large flux of protons
227 or light ions which are captured and formed into a beam by strong-focusing plasma lenses. The laser-
228 driven source allows protons and ions to be captured at energies significantly above those that pertain
229 in conventional facilities, thus evading the current space-charge limit on the instantaneous dose rate that
230 can be delivered. Rapid acceleration will be performed using a fixed-field alternating-gradient accelerator
231 (FFA) thereby preserving the unique flexibility in the time, energy, and spatial structure of the beam
232 afforded by the laser-driven source. Modern lasers are capable of delivering a Joule of energy in pulses
233 that are tens of femtoseconds in length at repetition rates of $\gtrsim 10$ Hz. At source, a laser-driven electron
234 beam is reproducibly-well collimated and has a modest ($\sim 5\%$) energy spread. Laser-driven ion sources
235 create beams that are highly divergent, have a large energy spread, and an intensity that can vary by up
236 to 40% pulse-to-pulse. These issues are addressed in the conceptual design through the use of plasma
237 lenses to provide strong focusing and to allow energy selection. In addition, sophisticated instrumentation
238 will be used in a fast feedback-and-control system to ensure that the dose delivered is both accurate and
239 reproducible. This approach will allow produce multiple ion species, from proton to carbon, to be produced
240 from a single laser by varying the target foil and particle-capture optics.

241 The LhARA consortium's vision is that LhARA will prove the principal of the novel technologies required
242 for the development of future therapy facilities. The legacy of the LhARA programme will therefore be:

- 243 • A unique facility dedicated to the development of a deep understanding of the radiobiology of proton
244 and ion beams; and
- 245 • The demonstration in operation of technologies that will allow PBT to be delivered in completely new
246 regimes.

247

3 THE LHARA FACILITY

248 The LhARA facility, shown schematically in figure 1, has been designed to serve two end stations for
249 *in vitro* radiobiology and one end station for *in vivo* studies. The principle components of the LhARA
250 accelerator are: the laser-driven proton and ion source; the matching and energy selection section; beam
251 delivery to the low-energy *in vitro* end station; the low-energy abort line; the injection line for the fixed-
252 field alternating-gradient accelerator (FFA); the FFA; the extraction line; the high-energy abort line; beam
253 delivery to the high-energy *in vitro* end station; and the transfer line to the *in vivo* end station. Proton beams
254 with energies of between 12 MeV and 15 MeV will be delivered directly from the laser-driven source to
255 the low-energy *in vitro* end station via a transfer line. The high-energy *in vitro* end station and the *in vivo*
256 end station will be served by proton beams with energy between 15 MeV and 127 MeV and by ion beams,
257 including C^{6+} with energies up to 33.4 MeV/u. This configuration makes it natural to propose that LhARA
258 be constructed in two stages; Stage 1 providing beam to the low-energy *in vitro* end station and Stage 2
259 delivering the full functionality of the facility. The development of LhARA Stage 1 will include machine
260 performance and optimisation studies designed to allow *in vitro* experiments to begin as soon as possible.

261 The design parameters for the various components of LhARA are given in tables 1 and 2. The design of
262 the LhARA facility is described in the sections that follow.

263

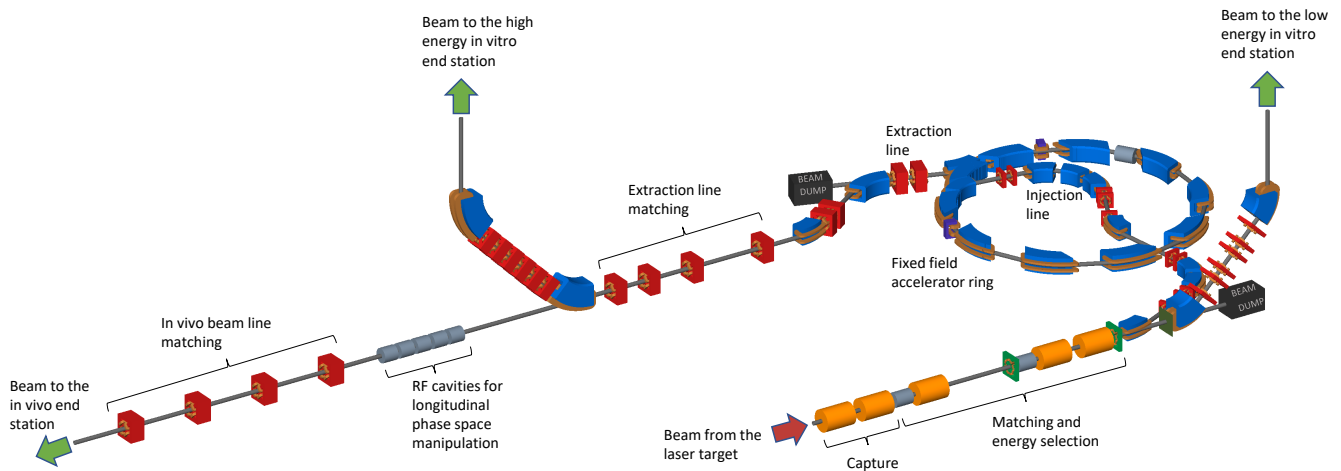


Figure 1. Schematic diagram of the LhARA beam lines. The particle flux from the laser-driven source is shown by the red arrow. The ‘Capture’ section is followed by the ‘Matching and energy selection’ section. The beam is then directed either into the 90° bend that takes it to the low-energy *in vitro* end station, towards the FFA injection line, or to the low-energy beam dump. Post acceleration is performed using the FFA on extraction from which the beam is directed either to the high-energy *in vitro* end station, the *in vivo* end station, or the high-energy beam dump.

Table 1. Design parameters of the components of the LhARA facility. The parameter table is provided in a number of sections. This section contains parameters for the Laser-driven proton and ion source, the Proton and ion capture section, and the Stage 1 beam transport section.

Parameter	Value or range	Unit
Laser driven proton and ion source		
Laser power	100	TW
Laser Energy	2.5	J
Laser pulse length	25	fs
Laser rep. rate	10	Hz
Required maximum proton energy	15	MeV
Proton and ion capture		
Beam divergence to be captured	50	mrad
Gabor lens effective length	0.857	m
Gabor lens length (end-flange to end-flange)	1.157	m
Gabor lens cathode radius	0.0365	m
Gabor lens maximum voltage	65	kV
Number of Gabor lenses	2	
Alternative technology: solenoid length	1.157	m
Alternative technology: solenoid max field strength	1.3	T
Stage 1 beam transport: matching & energy selection, beam delivery to low-energy end station		
Number of Gabor lenses	3	
Number of re-bunching cavities	2	
Number of collimators for energy selection	1	
Arc bending angle	90	Degrees
Number of bending magnets	2	
Number of quadrupoles in the arc	6	
Alternative technology: solenoid length	1.157	m
Alternative technology: solenoid max field strength (to serve the injection line to the Stage 2)	0.8 (1.4)	T

Table 2. Design parameters of the components of the LhARA facility. The parameter table is provided in a number of sections. This section contains parameters for the Stage 2 beam transport and the *in vitro* and *in vivo* end stations.

Parameter	Value or range	Unit
Stage 2 beam transport: FFA, transfer line, beam delivery to high-energy end stations		
Number of bending magnets in the injection line	7	
Number of quadrupoles in the injection line	10	
FFA: Machine type	single spiral scaling FFA	
FFA: Extraction energy	15–127	MeV
FFA: Number of cells	10	
FFA: Orbit R_{\min}	2.92	m
FFA: Orbit R_{\max}	3.48	m
FFA: Orbit excursion	0.56	m
FFA: External R	4	m
FFA: Number of RF cavities	2	
FFA: RF frequency	1.46–6.48	MHz
FFA: harmonic number	1, 2 or 4	
FFA: RF voltage (for 2 cavities)	4	kV
FFA: spiral angle	48.7	Degrees
FFA: Max B field	1.4	T
FFA: k	5.33	
FFA: Magnet packing factor	0.34	
FFA: Magnet opening angle	12.24	degrees
FFA: Magnet gap	0.047	m
FFA: Ring tune (x,y)	(2.83,1.22)	
FFA: γ_T	2.516	
FFA: Number of kickers	2	
FFA: Number of septa	2	
Number of bending magnets in the extraction line	2	
Number of quadrupoles in the extraction line	8	
Vertical arc bending angle	90	Degrees
Number of bending magnets in the vertical arc	2	
Number of quadrupoles in the vertical arc	6	
Number of cavities for longitudinal phase space manipulation	5	
Number of quadrupoles in the <i>in vivo</i> beam line	4	
<i>In vitro</i> biological end stations		
Maximum input beam diameter	1-3	cm
Beam energy spread (full width)	Low-energy end station: ≤ 4 High-energy end station: ≤ 1	% %
Input beam uniformity	< 5	%
Scintillating fibre layer thickness	0.25	mm
Air gap length	5	mm
Cell culture plate thickness	1.3	mm
Cell layer thickness	0.03	mm
Number of end stations	2	
<i>In vivo</i> biological end station		
Maximum input beam diameter	1-3	cm
Beam energy spread (full width)	≤ 1	%
Input beam uniformity	< 5	%
Beam options	Spot-scanning, passive scattering, micro-beam	

264 3.1 Laser-driven proton and ion source

265 Laser-driven ions have been posited as a source for radiobiological studies for a number of years [Kraft
266 et al. (2010); Yogo et al. (2011); Bin et al. (2012)]. Until now, the achievable ion energies, energy
267 spreads, and reproducibility of such beams have meant that such sources are not suitable for a full
268 radiobiological laboratory setting. While a number of cell irradiation experiments have been conducted
269 with laser-accelerated ions [Doria et al. (2012); Zeil et al. (2013); Pommarel et al. (2017); Manti et al.
270 (2017)], these have been limited in scope to a single-shot configuration. In addition, most of these
271 experiments have been performed on high-power laser facilities with rapidly shifting priorities, where the
272 time to install dedicated diagnostic systems has not been available. At present, a dedicated ion beam for
273 radiobiology, based on a laser-driven source, is not available anywhere in the world. Therefore, LhARA
274 will be a unique, state-of-the-art system, able to explore the radiobiological benefits of a laser-accelerated
275 ion source.

276 A novel solution for ion-acceleration is to use a compact, flexible laser-driven source coupled to a
277 state-of-the-art beam-transport line. This allows an accelerating gradient of $\gtrsim 10$ GV/m to be exploited at
278 the laser-driven source. We propose to operate in a laser-driven sheath-acceleration regime [Clark et al.
279 (2000); Snavely et al. (2000); Daido et al. (2012)] for ion generation. An intense, short laser pulse will
280 be focused onto a target. The intense electric field generated on the front surface of the target accelerates
281 the surface electrons, driving them into the material. Electrons which gain sufficient energy traverse the
282 target, ionising the material as they go. A strong space-charge electric field, the ‘sheath’, is created as the
283 accelerated electrons exit the rear surface of the target. This field in turn accelerates surface-contaminant
284 ions. The sheath-acceleration scheme has been shown to produce ion energies greater than 40 MeV/u at the
285 highest laser intensities. The maximum proton energy (E_p) scales with laser intensity (I) as, $E_p \propto I^{\frac{1}{2}}$. The
286 laser required to deliver a significant proton flux at 15 MeV can be compact, relatively inexpensive, and is
287 commercially available.

288 The distribution of proton and ion energies observed in laser-driven beams exhibits a sharp cut off at
289 the maximum energy and, historically, the flux of laser-accelerated ion beams has varied significantly
290 shot-to-shot. To reduce the impact of the shot-to-shot variations the choice has been made to select particles
291 from the plateau of the two-temperature energy spectrum of the laser-accelerated ion beam. This choice
292 should enhance ion-beam stability and allow reproducible measurements to be carried out at ultra-high dose
293 rates using a small number of fractions. To create the flux required in the plateau region it is proposed that
294 a 100 TW laser system is used. A number of commercial lasers are available that are capable of delivering
295 > 2.5 J in pulses of duration < 25 fs, at 10 Hz with contrast better than $10^{10} : 1$. Shot-to-shot stability of
296 $< 1\%$ is promised, an important feature for stable ion-beam production.

297 Key to the operation of this configuration is a system that refreshes the target material at high-repetition
298 rate in a reproducible manner. A number of schemes have been proposed for such studies, from high-
299 pressure gases [Willingale et al. (2009); Bin et al. (2015); Chen et al. (2017)], cryogenic hydrogen ribbons
300 [Margarone et al. (2016); Gauthier et al. (2017); Obst et al. (2017)], liquid sheets [Morrison et al. (2018)]
301 and tape drives [Noaman-ul Haq et al. (2017)]. For the LhARA facility, a tape drive based on the system
302 developed at Imperial College London is proposed. This system is capable of reliable operation at target
303 thicknesses down to $5 \mu\text{m}$, using both aluminium and steel foils, and down to $18 \mu\text{m}$ using plastic tapes.
304 Such tape-drive targets allow operation at high charge (up to 100 pC at 15 ± 1 MeV, i.e. $> 10^9$ protons per
305 shot) and of delivering high-quality proton and ion fluxes at repetition rates of up to 10 Hz or greater.

306 The unique features of the laser-driven ion source proposed for LhARA offer a number of opportunities
 307 to push the frontiers in the fields of sustained high-frequency ion generation, advanced targetry solutions
 308 and active, high-repetition rate diagnostics. The successful development and execution of LhARA will
 309 provide a leap forward in terms of capability and open up exciting new opportunities for applications not
 310 just in radiobiology. While pushing these new frontiers, the radiobiological-capabilities of LhARA are
 311 based on relatively low-energy ion beams, mitigating the risks that operating at the energy-frontier of the
 312 field would imply.

313 High repetition-rate operation of laser-driven radiation sources is a relatively new area of interest
 314 [Noaman-ul Haq et al. (2017); Aurand et al. (2019); Streeter et al. (2018); Dann et al. (2019); Kirschner
 315 et al. (2019)]. Such operating schemes pose a number of engineering challenges. It is proposed to apply
 316 machine-learning and genetic algorithms to the optimisation of the laser-target interaction to optimise the
 317 beam charge, peak energy, energy spread, and divergence of the ion flux produced [Aurand et al. (2019)].
 318 These techniques will require appropriate R&D effort. The first experiments of this kind will be possible
 319 using the existing laser capabilities at Imperial College London, the Central Laser Facility at the Rutherford
 320 Appleton Laboratory, and elsewhere.

321 The careful control of the tension on the tape in a tape-drive target is critical for reproducible operation.
 322 The tape must be stretched to flatten the surface, without stretching it to its plastic response. Surface
 323 flatness is important for a number of reasons. Rippling of the front surface modifies the laser absorption
 324 dramatically; uncharacterised rippling can make shot-to-shot variations significant and unpredictable
 325 [Noaman-ul Haq et al. (2017)]. Similarly, rear surface perturbations can modify the sheath field, resulting
 326 in spatial non-uniformities of the proton beam or suppression of the achievable peak energies. Tape drives
 327 with torsion control and monitoring to maintain a high-quality tape surface have been designed and operated
 328 in experiments at Imperial College London. The development of these targets continues with a view to the
 329 production of new, thinner tapes for improved ion generation and the creation of ion species other than
 330 proton and carbon. This is an active area of R&D that will continue with the development of LhARA.

331 High repetition-rate ion-beam diagnostics will also need to be developed. Such diagnostics will need to
 332 measure both the energy spectrum and the spatial profile of the beams. Current methods are destructive and
 333 are often limited to low-repetition rate. Passive detectors have not been demonstrated in the conditions that
 334 will pertain at LhARA. Technologies being evaluated to address the issues raised by ion-source diagnostics
 335 for LhARA are discussed in section 3.5.

336 3.2 Proton and ion capture 337

338 The use of an electron cloud as a focusing element for charged-particle beams was first proposed by
 339 Gabor in 1947 [Gabor (1947)]. Gabor noted that a cloud of electrons uniformly distributed about the axis
 340 of a cylindrical vessel would produce an ideal focusing force on a beam of positively charged particles. The
 341 focal length of such a lens scales with the energy of the incoming particle beam allowing such lenses to
 342 provide strong focussing of high-energy beams. Confinement conditions in the radial and axial directions
 343 can be determined [Pozimski and Aslaninejad (2013)]. In the radial direction, where there is magnetic
 344 confinement and Brillouin flow, the number density of electrons, n_e , that can be contained is given by:

$$n_e = \frac{\epsilon_0 B^2}{2m_e}; \quad (1)$$

345 where B is the magnetic field, m_e the mass of the electron, and ϵ_0 the permittivity of free space. In the
346 longitudinal direction there is electrostatic confinement for which n_e is given by:

$$n_e = \frac{4\epsilon_0 V_A}{eR^2}; \quad (2)$$

347 where e the magnitude of the charge on the electron and R is the radius of the cylindrical anode which
348 is held at the positive potential V_A . For the electron densities of interest for LhARA the required anode
349 voltage is of the order of 50 kV.

350 In the thin lens approximation, the focal length, f , of a Gabor lens can be expressed in terms of the
351 magnetic field and the particle velocity, v_p [Reiser (1989)]:

$$\frac{1}{f} = \frac{e^2 B^2}{4m_e m_p v_p^2} l; \quad (3)$$

352 where m_p is the mass of the particles in the beam. The focal length of the Gabor lens is therefore
353 proportional to the kinetic energy or, equivalently, the square of the momentum, of the incoming beam. By
354 comparison, the focal length for a solenoid is proportional to the square of the momentum and that of a
355 quadrupole is proportional to momentum. At the particle energies relevant to LhARA the Gabor lens, or
356 the solenoid, is therefore preferred.

357 An expression for the focal length as a function of electron number density can be derived by substituting
358 equation (1) into equation (3) to give:

$$\frac{1}{f} = \frac{e^3 n_e}{2\epsilon_0 U} l; \quad (4)$$

359 where $U = \frac{1}{2} m_p v_p^2$ is the kinetic energy of the particle beam. The focal length of the Gabor lens is inversely
360 proportional to the number density of electrons trapped in the cloud. The focal lengths desired to capture
361 the proton and ion beams at LhARA have been chosen such that the required electron number densities are
362 conservative and lie within the range covered in published experiments.

363 For a given focal length, the magnetic field required in the Gabor lens is reduced compared to that of a
364 solenoid that would give equivalent focusing. In the non-relativistic approximation the relationship between
365 the magnetic field in the Gabor lens, B_{GPL} , and the equivalent solenoid, B_{sol} , is given by [Pozimski and
366 Aslaninejad (2013)]:

$$B_{GPL} = B_{sol} \sqrt{Z \frac{m_e}{m_{ion}}}; \quad (5)$$

367 where m_{ion} is the mass of the ions being focused, and Z is the charge state of the ions. In the case of a
368 proton beam the reduction factor is 43. Thus, for example, where a 2 T superconducting solenoid would be
369 required, the magnetic field required for a Gabor lens would only be 47 mT. This means the cost of the
370 solenoid for a Gabor lens can be significantly lower than the cost for a solenoid of equivalent focusing
371 strength.

372 The plasma-confinement system described above is commonly known as a ‘Penning trap’ and has found
373 wide application in many fields [Thompson (2015)]. Variations on the Penning trap where axial apertures
374 in the cathodes are introduced, such as the Penning-Malmberg trap [deGrassie and Malmberg (1980);
375 Malmberg et al. (1988)] are attractive for beam-based applications due to the excellent access provided to
376 the plasma column, see figure 2.

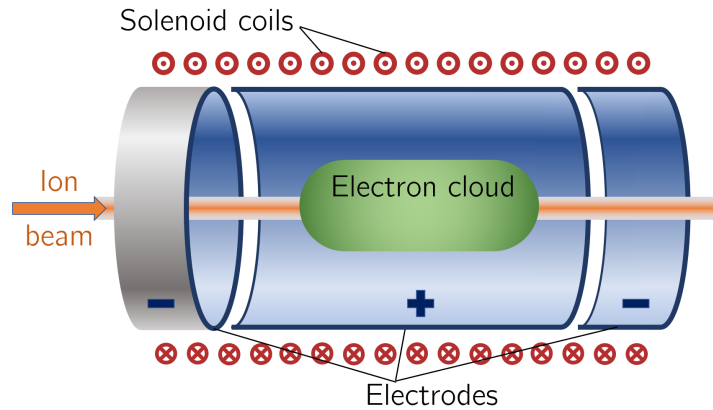


Figure 2. Schematic diagram of a Penning-Malmberg trap of the type proposed for use in the Gabor lenses to be used in LhARA. The solenoid coils, and the direction of current flow, are indicated by the red circles. The confining electrostatic potential is provided using a central cylindrical anode and two cylindrical negative end electrodes. The ion beam enters on-axis from the left and the electron cloud is indicated by the green shaded area.

377 Instability of the electron cloud is a concern in the experimental operation of Gabor lens; azimuthal beam
 378 disruption due to the diocotron instability has been observed and described theoretically [Meusel et al.
 379 (2013)]. Theory indicates that the diocotron instability is most problematic under well-defined geometric
 380 conditions. The reliable operation of a Gabor lens in a regime free from this instability has yet to be
 381 demonstrated. Gabor lenses promise very strong focusing, simple construction, and low magnetic field,
 382 all attractive features for LhARA. However, these attractive features come at the cost of relatively high
 383 voltage operation ($\gtrsim 50$ kV) and possible vulnerability to instability.

384 With reliable operation of Gabor lenses as yet unproven, we plan a two-part experimental and theoretical
 385 programme of research to prove Gabor-lens suitability. Initial work will include: theoretical investigation
 386 of lens stability in a full 3D particle-in-cell code such as VSIM [VSI (2020)]; and the development of
 387 electron-density diagnostics based on interferometric measurement of the refractive-index change. These
 388 activities will be applied to a time-invariant electron cloud. A test Gabor lens will be constructed to allow
 389 validation of both the simulation results and a new diagnostic using an alpha emitter as a proxy for the
 390 LhARA beam. In addition, the initial investigation will include the design of an electron beam to fill the
 391 lens. This last objective will enable the second part of the experimental project; the operation of the Gabor
 392 lens in short pulses. It is attractive to match the timing of the establishment of the electron cloud within the
 393 Gabor lens to that of the beam and thereby limit instability growth. The research project is time limited
 394 such that, should it not prove possible to produce a suitable Gabor lens, there will remain time sufficient to
 395 procure conventional solenoids in their place.

396

397 **3.3 Beam transport and delivery to the low-energy *in vitro* end station**

398 Beam-transport from the laser-driven ion source and delivery to the low-energy *in vitro* end station is
 399 required to deliver a uniform dose distribution at the cell layer. Beam losses must be minimised for radiation
 400 safety and to maximise the dose that can be delivered in a single shot. The transport line has been designed
 401 to minimise regions in which the beam is brought to a focus to reduce the impact of space-charge forces on
 402 the beam phase-space. An optical solution was initially developed using Beamoptics [Autin et al. (1998)]
 403 and MADX [Grote and Schmidt (2003)]. Accurate estimation of the performance of the beam line requires

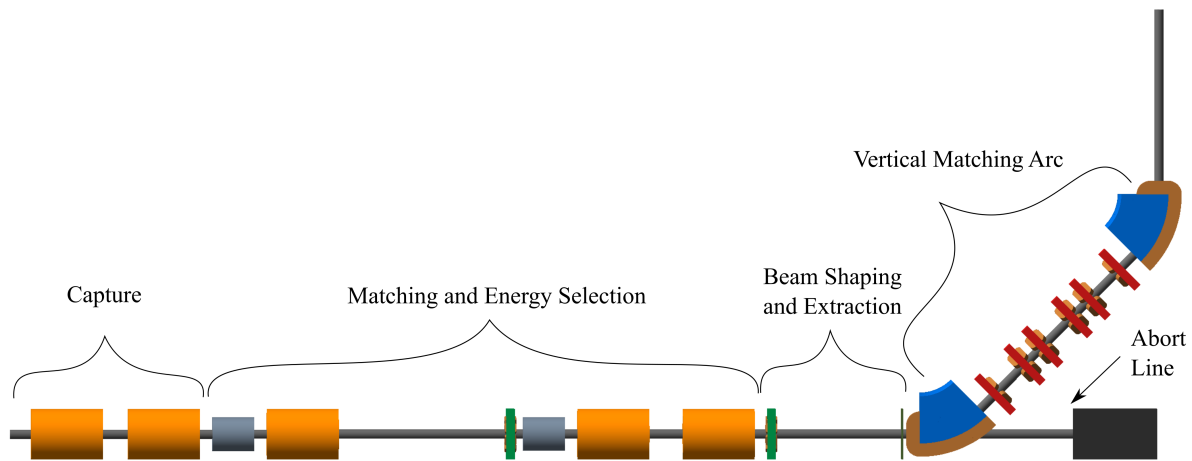


Figure 3. Beam transport for Stage 1 of LhARA visualised in BDSIM, showing five machine sections. The capture section is composed of two Gabor lenses (orange cylinders). The matching and energy selection section includes three Gabor lenses, two RF cavities (grey cylinders) and an octupole magnet (green disc). The beam shaping and extraction section includes a second octupole and a collimator (black vertical bar). The vertical matching arc directs the beam into the low-energy *in vitro* end station and is composed of two 45° dipoles and six quadrupoles. The total length of this beam line is 17.255 m.

404 the inclusion of space-charge forces and particle-matter interactions. Therefore, performance estimation
 405 was performed using Monte Carlo particle-tracking from the ion source to the end station. BDSIM [Nevay
 406 et al. (2020)], which is based on the Geant4 toolkit was used for the simulation of energy deposition arising
 407 from beam interactions with the material in the accelerator and the end station. GPT [De Loos and Van der
 408 Geer (1996)] was used for evaluating the full 3D impact of space-charge.

409 An idealised Gaussian beam was generated with a spot size of $4\ \mu\text{m}$ FWHM, an angular divergence of
 410 $50\ \text{mrad}$, $35\ \text{fs}$ FWHM bunch length, and an energy spread of $1 \times 10^{-6}\ \text{MeV}$. The maximum estimated
 411 bunch charge is 1×10^9 protons. The presence of a substantial electron flux produced from the laser target
 412 compensates the high proton charge density in the vicinity of the ion-production point. Therefore, the first
 413 $5\ \text{cm}$ of beam propagation was simulated without space-charge. Beyond this, the proton beam will have
 414 separated from the lower energy electrons sufficiently for space-charge to become a prominent effect and
 415 cause an emittance growth. Therefore, a further $5\ \text{cm}$ drift was simulated including space-charge forces. At
 416 a distance of $10\ \text{cm}$ from the ion source the beam is at the exit of the laser-target vessel. The kinematic
 417 distributions of ions in the beam were stored at this point and passed to the relevant BDSIM and GPT
 418 simulations of the downstream beam line.

419 The beam line, shown schematically in figure 3, is composed of five sections: beam capture; matching
 420 and energy selection; beam shaping; vertical arc matching; and an abort line. The capture section uses two
 421 Gabor lenses to minimise the transverse momentum of particles in the beam. Beyond the capture section,
 422 an RF cavity permits control of the bunch length and manipulation of the longitudinal phase-space. A third
 423 Gabor lens then focuses the bunch to a small spot size after which a second RF cavity is located to provide
 424 further longitudinal phase-space manipulation. Two further Gabor lenses bring the beam parallel once more
 425 in preparation for the vertical 90° arc. All Gabor lenses have an inner radius of $3.65\ \text{cm}$ and an effective
 426 length of $0.857\ \text{m}$. All lenses operate below the maximum cathode voltage of $65\ \text{kV}$.

427 A parallel beam emerges from the final Gabor lens, providing significant flexibility for the inclusion of
428 beam shaping and extraction systems. Beam uniformity will be achieved using octupole magnets to provide
429 third-order focusing to perturb the first-order focusing from the Gabor lenses. Such schemes have been
430 demonstrated in a number of facilities [Tsoupas et al. (1991); Urakabe et al. (1999); Amin et al. (2018)].
431 A suitable position for the first octupole was identified to be after the final Gabor lens where the beam is
432 large; its effect on the beam is expected to be significant. Octupoles were only modelled in BDSIM as GPT
433 does not have a standard component with an octupolar field. The typical rectangular transverse distribution
434 resulting from octupolar focusing requires collimation to match the circular aperture through which the
435 beam enters the end station. A collimator is therefore positioned at the start of the vertical arc. Further
436 simulations are required to determine the optimum position of the second octupole and to evaluate the
437 performance of the octupoles. The switching dipole which directs the beam to the injection line of the FFA
438 in Stage 2 will be located between the second octupole and the collimator, requiring the octupole to be
439 ramped down for Stage 2 operation.

440 The vertical arc uses transparent optics in an achromat matching section to ensure that the first-order
441 transfer map through the arc is equivalent to the identity transformation and that any dispersive effects are
442 cancelled. A 2 m drift tube is added after the arc to penetrate the concrete shielding of the end station floor
443 and to bring the beam to bench height. The abort line consists of a drift followed by a beam dump and
444 requires the first vertical dipole to ramp down, preventing charged-particle transportation to the end station.

445 The underlying physics of plasma-lens operation cannot be simulated in BDSIM or GPT, however it
446 can be approximated using solenoid magnets of equivalent strength. RF cavity fields were not simulated.
447 10 000 particles were simulated corresponding to the estimated maximum bunch charge of 1×10^9 protons.
448 Figure 4 shows excellent agreement between horizontal and vertical transverse beam sizes in BDSIM
449 and MADX, verifying the beam line's performance in the absence of space-charge effects. Reasonable
450 agreement between BDSIM and GPT is also seen when space-charge forces are included in GPT. Emittance
451 growth is observed prior to the first solenoid, affecting the optical parameters throughout the machine.
452 However, the resulting beam dimensions at the cell layer of 1.38 cm horizontally and 1.47 cm vertically
453 are not significantly different from the ideal beam in BDSIM. Further adjustments of the Gabor lenses
454 and arc-quadrupole strengths may compensate for this. The transmission efficiency of the beam line is
455 approximately 100%.

456 The small bunch dimensions in both transverse planes at the focus after the third Gabor lens, where
457 the energy selection collimator will be placed, remains a concern if the effect of space-charge has been
458 underestimated. Similar bunch dimensions are achieved in the vertical arc, however, quadrupolar focusing
459 is confined to a single plane mitigating further emittance growth. Further tuning of the Gabor lens voltages
460 in the capture section may compensate space-charge effects, reducing the non-zero transverse momentum
461 seen entering the vertical arc.

462 To investigate beam uniformity, BDSIM simulations with and without octupoles and collimation for beam
463 shaping were conducted. Both octupoles were arbitrarily set to a strength of $K3 = 6000$ with a magnetic
464 length of 0.1 m and pole-tip radius of 5 cm, which, for a 15 MeV beam corresponds to pole-tip field of
465 0.42 T. A 2 cm thick iron collimator with a 40 mm diameter aperture was positioned 1.5 m downstream
466 of the octupole. Figure 5 shows the beam phase-space and particle distributions at the end station for the
467 transverse and longitudinal axes with and without beam shaping. Without octupoles the spatial profile
468 is Gaussian as expected, however, beam uniformity is improved with octupoles and collimation. The
469 total beam width is 3.58 cm horizontally and 3.46 cm vertically which is sufficient to irradiate one well
470 in a six-well cell-culture plate. Further optimisation is required to improve uniformity whilst optimising

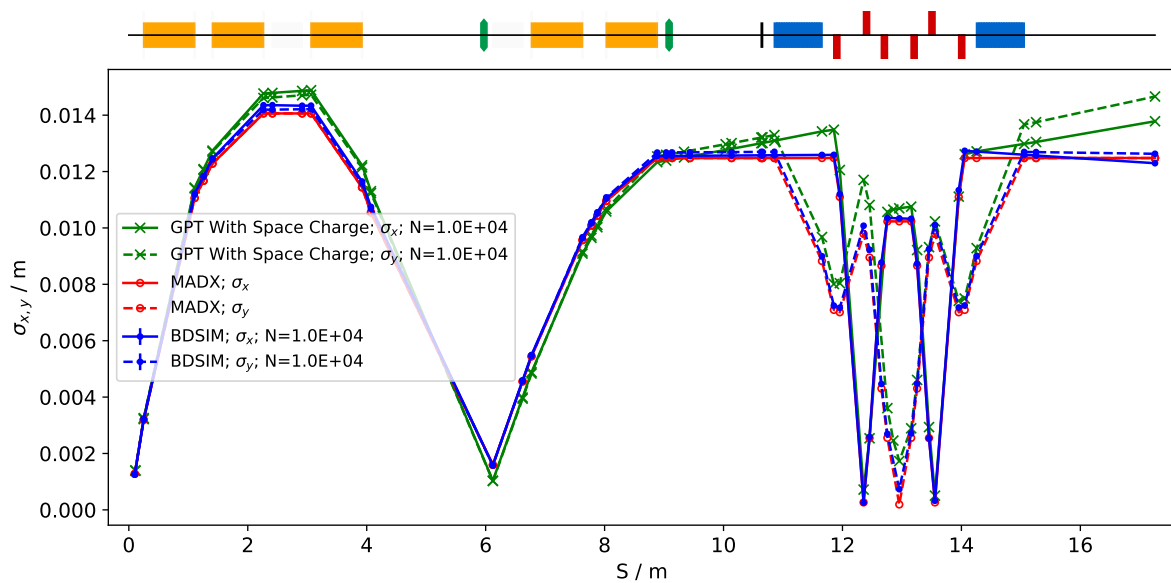


Figure 4. Horizontal (solid lines) and vertical (dashed lines) beam sizes through the *in vitro* beam transport, simulated with space-charge in GPT (green), and without space-charge in MADX (red) and BDSIM (blue).

471 beam-line transmission, which is approximately 70% for the results presented in figure 5. An aberration
 472 can be seen in both transverse planes with and without beam shaping; this effect originates upstream of
 473 the octupoles in the solenoids, and persists through to the end station. These aberrations are a concern,
 474 however, future simulation efforts will replace the solenoids with a full electromagnetic simulation of the
 475 Gabor lens. This change is likely to change the aberrations. The non-Gaussian energy distribution without
 476 beam shaping is a result of space-charge forces at the ion source; the distribution persists to the end station
 477 as no components which affect the longitudinal phase space were simulated. The Gaussian distribution
 478 seen with beam shaping is due to collimation.

479 The proposed design is capable of delivering beams of the desired size to the *in vitro* end station. Space-
 480 charge effects impact the beam-transport performance but it is believed that this can be mitigated with
 481 minor adjustments to the Gabor lenses in the capture section. Initial studies indicate that a uniform beam
 482 can be delivered with further optimisation of the octupoles and collimator.

483 484 3.3.1 Alternative Design

485 To mitigate potential emittance growth from space-charge forces, an alternative beam line design was
 486 developed in which the final two Gabor lenses in the matching and energy selection section are replaced by
 487 four quadrupoles, limiting any bunch focusing to one plane at a time. The resulting machine is reduced
 488 in length to 15.439 m. Without space-charge effects, a beam sigma of 2.5 mm at the end station can be
 489 achieved. With space-charge, emittance growth prior to the first solenoid is once again observed leading
 490 to an increased beam size at the entrance of the first quadrupole, resulting in a spatially asymmetric and
 491 divergent beam at the end station. It is believed that the space-charge effects can be compensated by
 492 applying the same Gabor-lens optimisation as in the baseline design and adjusting the quadrupole settings
 493 to deliver beam parameters similar to those without achieved in the absence of space charge. The alternative
 494 design provides a solution that is more resilient to space-charge effects than the baseline, however, only the
 495 lower bound on the desired beam size has been achieved so far. Further optimisation is required not only to

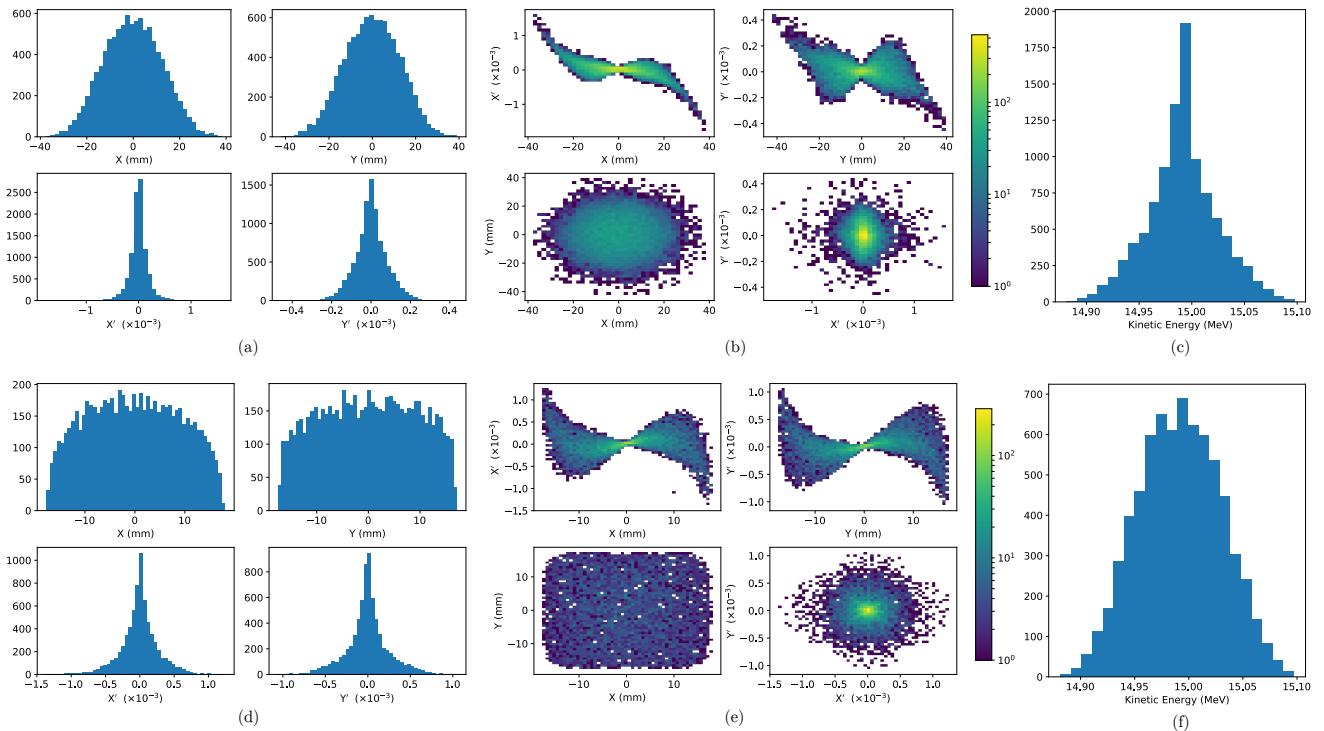


Figure 5. Beam phase space distributions at the end-station in the transverse plane, (X, Y) ; X' and Y' give the slope relative to the Z axis. The transverse phase space is shown in figures a and b for simulations without octupolar focusing and collimation, with the kinetic energy distribution shown in c. The same phase space distributions simulated with the effect of octupoles and collimation are in figures d, e, and f.

496 optimise optical performance but also to optimise octupole settings and to determine whether a beam with
 497 the desired uniformity can be delivered to the end station.

498 3.4 Post-acceleration and beam delivery to the *in vitro* and *in vivo* end stations

500 A fixed-field alternating-gradient accelerator (FFA), based on the spiral scaling principle [Krest et al.
 501 (1956); Symon et al. (1956); Fourier et al. (2008); Tanigaki et al. (2006)], will be used to accelerate the
 502 beam in LhARA Stage 2 to obtain energies greater than the 15 MeV protons and 4 MeV/u carbon (C^{6+})
 503 ions delivered by the laser-driven source. FFAs have many advantages for both medical and radiobiological
 504 applications such as: the capability to deliver high and variable dose; rapid cycling with repetition rates
 505 ranging from 10 Hz to 100 Hz or beyond; and the ability to deliver various beam energies without the use
 506 of energy degraders. An FFA is relatively compact due to the use of combined function magnets, which
 507 lowers the overall cost compared to conventional accelerators capable of delivering beams at a variety of
 508 energies such as synchrotrons. Extraction can be both simple and efficient and it is possible for multiple
 509 extraction ports to be provided. Furthermore, FFAs can accelerate multiple ion species, which is very
 510 important for radiobiological experiments and typically very difficult to achieve with cyclotrons.

511 A typical FFA is able to increase the beam momentum by a factor of three, though a greater factor may
 512 be achieved. For LhARA, this translates to a maximum proton-beam energy of 127 MeV from an injected
 513 beam of 15 MeV. For carbon ions (C^{6+}) with the same rigidity, a maximum energy of approximately
 514 33.4 MeV/u can be produced.

515 The energy at injection into the FFA determines the beam energy at extraction. The injection energy will
 516 be changed by varying the focusing strengths in the Stage 1 beam line from the capture section through to
 517 the extraction line and the FFA ring. This will allow the appropriate energy slice from the broad energy
 518 spectrum produced at the laser-driven source to be captured and transported to the FFA. The FFA will then
 519 accelerate the beam, acting as a three-fold momentum multiplier. This scheme simplifies the injection and
 520 extraction systems since their geometry and location can be kept constant.

521 A second, ‘high-energy’, *in vitro* end station will be served by proton beams with a kinetic energy in the
 522 range 15–127 MeV and carbon-ion beams with energies up to 33.4 MeV/u. The extraction line from the
 523 FFA leads to a 90° vertical arc to send the beam to the high-energy *in vitro* end station. If the first dipole
 524 of the arc is not energised, beam will be sent to the *in vivo* end station. The extraction line of the FFA
 525 includes a switching dipole that will send the beam to the high-energy-beam dump if it is not energised.
 526 The detailed design of the high-energy abort line, taking into account the requirement that stray radiation
 527 does not enter the end stations, will be performed as part of the LhARA R&D programme.

528

529 3.4.1 Injection line

530 The settings of the Stage 1 beam line need to be adjusted to reduce the Twiss β function propagating
 531 through the injection line to allow beam to be injected into the FFA ring. The optical parameters in the
 532 Stage 1 beam line after adjustment are shown in figure 6. The beam is diverted by a switching dipole into
 533 the injection line which transports the beam to the injection septum magnet. The injection line matches
 534 the Twiss β functions in both transverse planes and the dispersion of the beam to the values dictated by
 535 the periodic conditions in the FFA cell (figure 6). The presence of dispersion in the injection line allows a
 536 collimator to be installed for momentum selection before injection. The beam is injected from the inside of
 537 the ring, which requires the injection line to cross one of the straight sections between the FFA magnets,
 538 see figure 7.

539

540 3.4.2 FFA ring

541 The magnetic field, B_y , in the median plane of a scaling spiral FFA is given by [Krest et al. (1956); Symon
 542 et al. (1956); Fourrier et al. (2008)]:

$$B_y = B_0 \left[\frac{R}{R_0} \right]^k F \left(\theta - \ln \left[\frac{R}{R_0} \right] \tan \zeta \right); \quad (6)$$

543 where B_0 is the magnetic field at radius R_0 , k is the field index, ζ corresponds to the spiral angle and F
 544 is the ‘flutter function’. This field law defines a zero-chromaticity condition, which means the working
 545 point of the machine is independent of energy up to field errors and alignment imperfections. This avoids
 546 crossing any resonances, which would reduce the beam quality and may lead to beam loss.

547 Table 2 gives the main design parameters of the FFA ring. The ring consists of ten symmetric cells each
 548 containing a single combined-function spiral magnet. The choice of the number of cells is a compromise
 549 between the size of the orbit excursion, which dictates the radial extent of the magnet, and the length of the
 550 straight sections required to accommodate the injection and extraction systems.

551 The betatron functions and dispersion in one lattice cell at injection are shown in figure 8a. The tune
 552 diagram, showing the position of the working point of the machine in relation to the main resonance
 553 lines, is shown in figure 8b. Tracking studies were performed using a step-wise tracking code in which the
 554 magnetic field is integrated using a Runge-Kutta algorithm [Lagrange et al. (2018)]. The magnetic field in

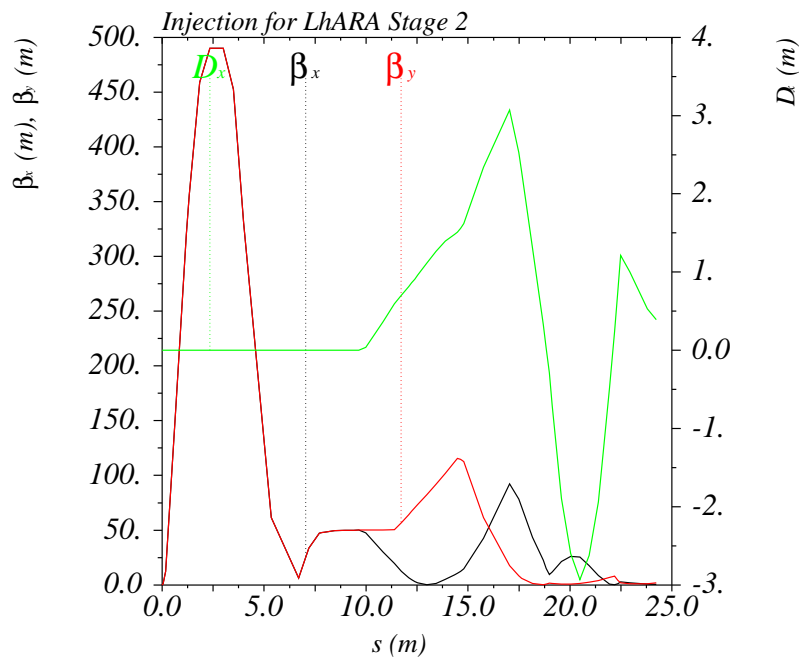


Figure 6. Twiss β_x and β_y functions and dispersion in the beam line consisting of the modified Stage 1 lattice and the transfer line allowing injection of the beam into the FFA ring. S goes from the laser target to the exit of the injection septum.

555 the median plane was obtained using the ideal scaling law (equation 6) and using using Enge functions to
 556 give the fringe fields. The field out of the median plane was obtained using Maxwell's equations and a
 557 6th-order Taylor expansion of the field. The dynamic acceptance for 100 turns, shown for the horizontal
 558 and vertical planes in figures 8c and 8d respectively, are significantly larger than the beam emittance. This
 559 statement holds even when the most pessimistic scenario, in which the emittance is assumed to be ten times
 560 larger than nominal, is used. These results confirm that a good machine working point has been chosen.

561 A full aperture, fast injection of the beam will be performed using a magnetic septum, installed on the
 562 inside of the ring, followed by a kicker magnet situated in a consecutive lattice cell, as shown in figure 7.
 563 The specifications of the injection system are dictated by the parameters of the beam at injection, which are
 564 summarised for the nominal proton beam in table 3. The beam at injection has a relatively small emittance
 565 and short bunch length, which limits the intensity accepted by the ring due to the space-charge effect. An
 566 intensity of approximately 10^9 protons will be accepted by the ring assuming the nominal beam parameters.
 567 Space-charge effects will be severe immediately after injection, but will quickly be reduced due to the
 568 debunching of the beam. Fast extraction of the beam over the full aperture will be performed using a kicker
 569 magnet followed by a magnetic septum installed in a consecutive lattice cell close to the extraction orbit.

570 Acceleration of the beam to 127 MeV will be done using an RF system operating at harmonic number
 571 $h = 1$ with an RF frequency range from 2.89 MHz to 6.48 MHz. The RF voltage required for 10 Hz
 572 operation is 0.5 kV. However, at such a low voltage the energy acceptance at injection will be limited to
 573 $\pm 0.7\%$ so a voltage of 4 kV is required to increase the energy acceptance to $\pm 2\%$. This voltage can be
 574 achieved with one cavity [Yonemura et al. (2008)], two cavities are assumed to provide greater operational
 575 stability. Normal conducting spiral-scaling FFA magnets, similar to the ones needed for LhARA, have

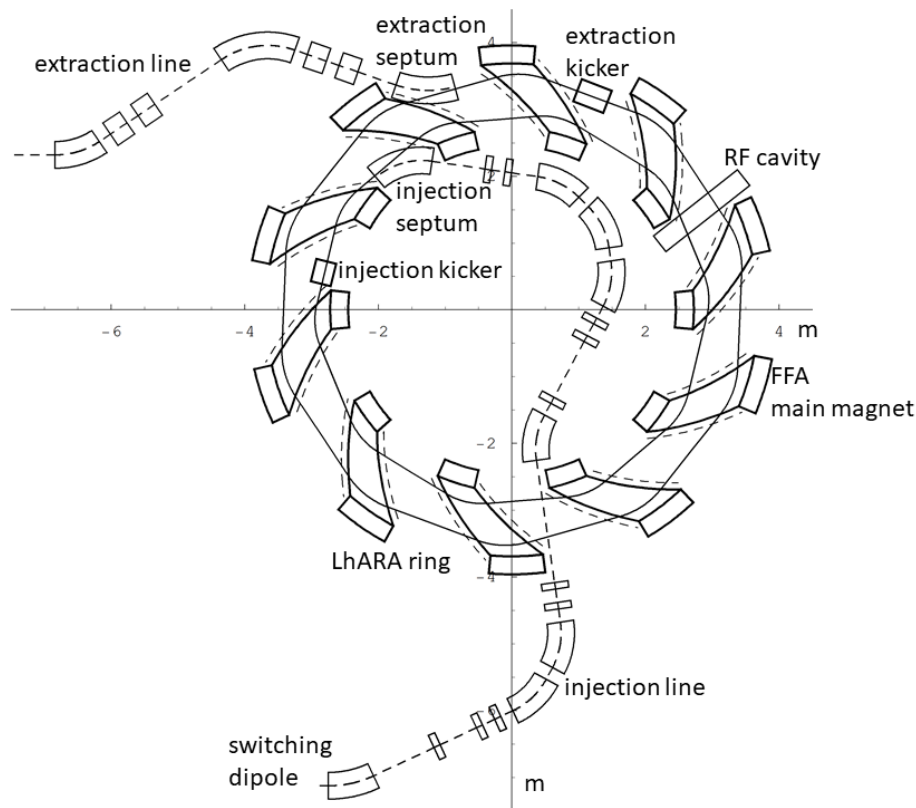


Figure 7. The layout of the injection line from the switching dipole to the injection septum together with the FFA ring, some of its subsystems and the first part of the extraction line.

Table 3. Summary of the main parameters for the proton beam at the injection to the FFA ring. These parameters correspond to the nominal (maximum) acceleration mode of operation.

Parameter	Unit	Value
Beam energy	MeV	15
Total relative energy spread	%	± 2
Nominal physical RMS emittance (both planes)	π m rad	4.1×10^{-7}
Incoherent space charge tune shift		-0.8
Bunching factor		0.023
Total bunch length	ns	8.1
Bunch intensity		10^9

576 been constructed successfully [Tanigaki et al. (2006); Planche et al. (2009)] using either distributed,
 577 individually-powered coils on a flat pole piece or using a conventional gap-shaping technique. For the
 578 LhARA FFA, we propose a variation of the coil-dominated design recently proposed at the Rutherford
 579 Appletton Laboratory in R&D studies for the upgrade of the ISIS neutron and muon source. In this case, the
 580 nominal scaling field is achieved using a distribution of single-powered windings on a flat pole piece. The
 581 parameter k can then be tuned using up to three additional independently-powered windings. The extent
 582 of the fringe field across the radius of the magnet must be carefully controlled using a ‘field clamp’ to
 583 achieve zero-chromaticity. An active clamp, in which additional windings are placed around one end of the
 584 magnet, may be used to control the flutter function and thereby vary independently the vertical tune of the
 585 FFA ring. The FFA is required to deliver beams over a range of energy; each energy requiring a particular

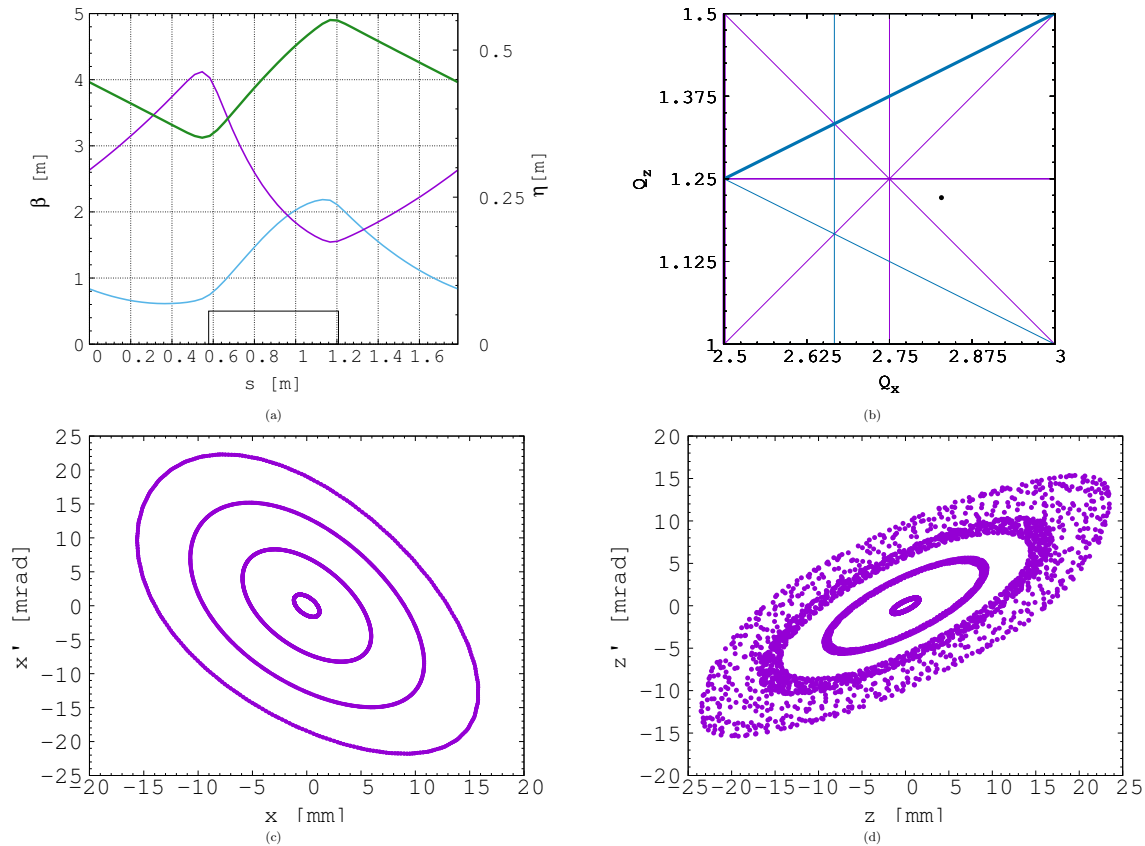


Figure 8. Beam optics and tracking in the FFA. Twiss β_h (blue), β_v (purple) functions and dispersion (green) in one lattice cell of the FFA ring (a). The working point of the FFA ring at (2.83, 1.22) on the tune diagram (b). The results of the horizontal (c) and vertical (d) dynamical acceptance study in the FFA ring, where a 1 mm offset is assumed in the vertical and horizontal planes respectively.

586 setting for the ring magnets. Therefore, a laminated magnet design may be required to reduce the time
 587 required to change the field. The magnet gap of 4.7 cm given in table 2 is estimated assuming a flat-pole
 588 design for the magnet. The details of the design will be addressed in as part of the LhARA R&D programme.
 589

590 3.4.3 Extraction Line

591 Substantial margins in the beam parameters were assumed in the design of the extraction line from the
 592 FFA due to uncertainties in the beam distributions originating from: the Stage 1 beam transport; the
 593 FFA injection line; and potential distortions introduced by the presence of space-charge effects during
 594 acceleration in the ring. Therefore, the beam emittance was allowed, pessimistically, to be as large as a
 595 factor of ten greater than in the nominal value, which was derived assuming that the normalised emittance
 596 is conserved from the source, through the Stage 1 beam line, and in the FFA ring. In the nominal case,
 597 the physical emittance of the beam is affected by adiabatic damping only. Substantial flexibility in the
 598 optics of the extraction line is required, as the extraction line must accommodate a wide spectrum of beam
 599 conditions to serve the *in vitro* and *in vivo* end-stations.

600 Detailed studies were carried out for proton beams with kinetic energies of 40 MeV and 127 MeV. Table
 601 4 gives the Twiss β values for different beam sizes for the 40 MeV and 127 MeV proton-beam scenarios
 602 assuming a Gaussian beam distribution. The optics and geometric acceptance of the system is approximately
 603 the same for the 40 MeV and 127 MeV beams. This justified the working hypothesis that beam emittance is

Table 4. Beam emittance values and target β values for different beam sizes for 40 MeV and 127 MeV beams. The beam size is taken to be four times the sigma of the transverse beam distribution.

	40 MeV protons (Nominal)	127 MeV protons (Nominal)	127 MeV protons (Pessimistic)
RMS Emittance (ϵ_x, ϵ_y) [π mm mrad]	0.137	0.137	1.37
β [m] for a 1 mm spot size	0.46	0.46	0.039
β [m] for a 10 mm spot size	46	46	4.5
β [m] for a 30 mm spot size	410	410	40

604 approximately the same for both beam energies. This assumption will be revised as soon as space-charge
605 simulations for the entire system are available.

606 The first two dipoles and four quadrupoles of the extraction line bend the beam coming from the extraction
607 septum of the FFA such that it is parallel to the low-energy beam line while ensuring that dispersion is
608 closed. Closing the dispersion is critical as off-momentum particles will follow trajectories different to
609 those followed by particles with the design momentum and therefore impact the size and shape of the beam
610 downstream. The second part of the extraction line consists of four quadrupoles which transport the beam
611 either to the first dipole of the vertical arc that serves the high-energy *in vitro* end station or to the *in vivo*
612 end-station if this dipole is not energised. These quadrupoles provide the flexibility required to produce the
613 different beam sizes for the *in vitro* end station as specified in table 4.

614

615 3.4.4 High-energy *in vitro* beam line

616 The high-energy *in vitro* beam line transports the beam from the exit of the extraction line and delivers it to
617 the high-energy *in vitro* end station. The 90° vertical bend is a scaled version of the low-energy vertical arc,
618 following the same design principles, and also consists of two bending dipole magnets and six quadrupole
619 magnets. To accommodate the higher beam energies, the lengths of the magnets were scaled in order to
620 ensure that peak magnetic fields were below the saturation limits of normal conducting magnets. The
621 bending dipole magnet lengths were increased to 1.2 m each and the quadrupole lengths were tripled to
622 0.3 m each. The overall length of the arc then becomes 6 m, compared to 4.6 m for the low energy *in vitro*
623 arc. This difference in arc length means the high-energy *in vitro* arc finishes about 0.9 m higher than the
624 low-energy one. This difference can easily be accommodated by adjusting the final drift lengths.

625 The quadrupole strengths for the scaled high-energy *in vitro* arc were obtained using MAD-X and
626 tracking simulations using BDSIM show good agreement, see figure 9. The input beam distribution used
627 in BDSIM was assumed to be Gaussian with Twiss $\beta = 46$, which gives a beam size of about 10 mm.
628 GPT simulations were performed which show small discrepancies due to space-charge effects. It may be
629 possible to compensate for this by adjusting the strengths of the quadrupoles in the arc and the matching
630 section in the extraction line.

631

632 3.4.5 *In vivo* beam line

633 If the first dipole of the high-energy *in vitro* arc is not energised then beam is sent to the *in vivo* end station.
634 From the end of the extraction line, 7.7 m of drift is necessary to clear the first bending dipole of the *in*
635 *vitro* arc, to provide space for the five RF cavities needed for longitudinal phase-space manipulation and to
636 allow space for diagnostic devices. Following this drift is a further 6.6 m of beam line that includes four
637 quadrupoles, each of length 0.4 m, which are used to perform the final focusing adjustments of the beam
638 delivered to the *in vivo* end station. A final 1.5 m drift at the end is reserved for scanning magnets to be

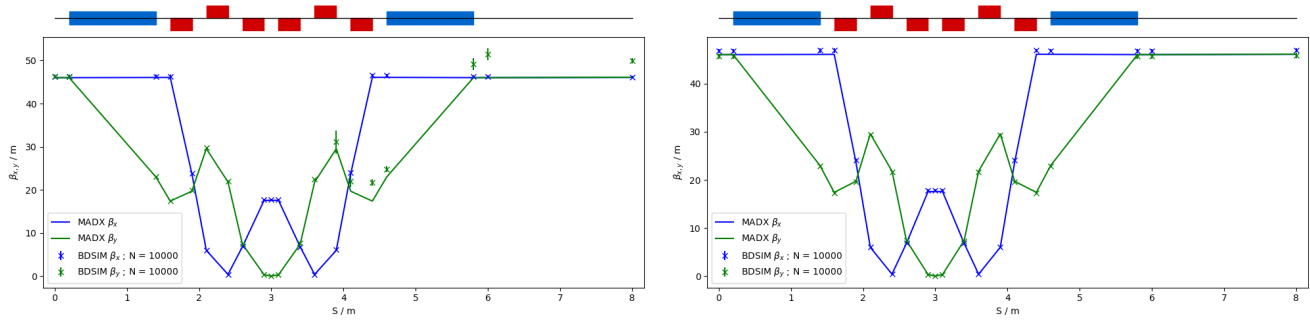


Figure 9. Comparison of MAD-X and BDSIM simulation of 40 MeV (left) and nominal 127 MeV (right) proton beam passing through the high energy *in vitro* arc simulated with 10^4 particles (in BDSIM).

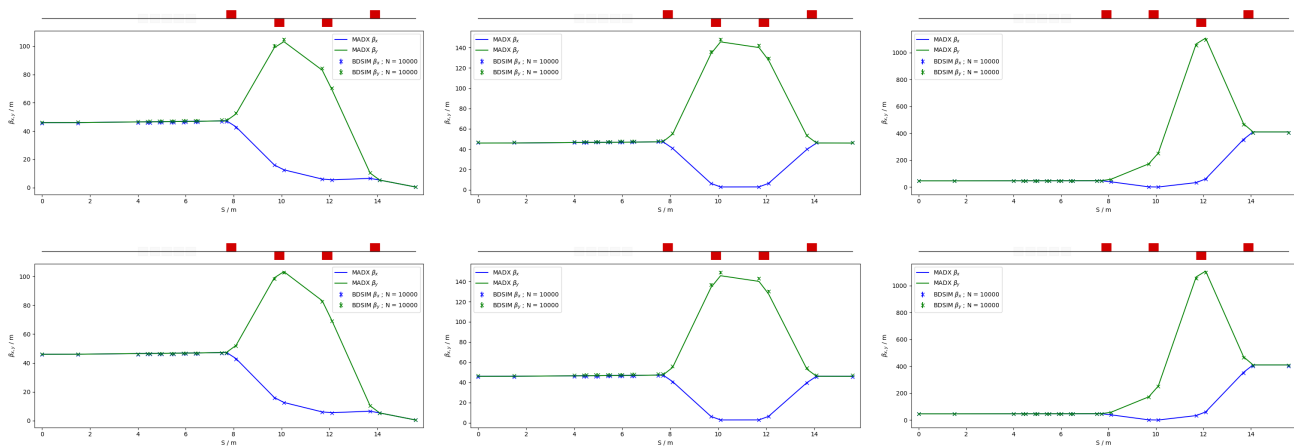


Figure 10. MAD-X and BDSIM simulations of the *in vivo* beam line for a 40 MeV proton beam (top row) and a nominal 127 MeV proton beam (bottom row) with quadrupoles matched to $\beta_{x,y} = 0.46$ m (left), $\beta_{x,y} = 46$ m (middle) and $\beta_{x,y} = 410$ m (right) for 10^4 particles.

639 installed to perform spot scanning and to penetrate the shielding of the *in vivo* end station. In total the *in*
 640 *in vivo* beam line is 15.6 m in length.

641 The design is flexible in matching the various $\beta_{x,y}$ values given in table 4, but is not able to match
 642 the smallest target value of $\beta_{x,y} = 0.039$ m for the pessimistic scenario, which is very challenging. To
 643 verify that the optics design could provide the required beam sizes, simulations were performed with
 644 BDSIM using an input Gaussian beam generated with the Twiss β values given in tables 4. Figure 10
 645 shows the results of simulations for a 40 MeV proton beam and a nominal emittance 127 MeV proton
 646 beam matched in order to obtain beam sizes of 1 mm, 10 mm and 30 mm. GPT was used to investigate the
 647 effects of space-charge. These simulations show discrepancies compared to the BDSIM simulations. These
 648 discrepancies can be compensated for by adjusting the strengths of the quadrupoles in the matching section
 649 in the extraction line.

650

651 3.5 Instrumentation

652 Commercial off-the-shelf (COTS) instrumentation will be used for Stages 1 and 2 of LhARA wherever
 653 possible. However, the characteristics of the beam (e.g. very high charge-per-bunch, low-to-moderate
 654 energy) will require some custom solutions to be developed. The authors are developing two concepts,
 655 termed SciWire and SmartPhantom, for the low- and high-energy *in vitro* end stations respectively. These

656 detectors can also be used for beam diagnostics. This new instrumentation may find application at other
657 facilities. Instrumentation for the detection of secondary particles arising from the interaction of the beam
658 with tissue is not discussed here but is an important area that will be studied in the future.

659 3.5.1 SciWire 660

661 For the Stage 1 beam, the maximum proton energy is 15 MeV. Shot-to-shot characterisation of the beam is
662 essential and requires the use of a very thin detector with a fast response. The SciWire [Kurup (2019)] is
663 being developed to provide energy and intensity profile measurements for low-energy ion beams. A single
664 SciWire plane consists of two layers of 250 μm square-section scintillating fibres, with the fibre directions
665 in the two layers orthogonal to each other. A series of back-to-back planes provides a homogeneous volume
666 of scintillator. If there are enough planes to stop the beam, the depth of penetration will allow the beam
667 energy to be inferred. This is obviously a destructive measurement so it is envisaged that this type of
668 measurement would only be used when experiments are not running. A single plane, however, can be used
669 for 2D beam-profile measurements at the same time that beam is delivered for experiments. Detection of
670 the light from SciWire fibres may be by CMOS camera, or using photodiodes. If the instrumentation is
671 sufficiently fast, the SciWire can be used to derive feedback signals for beam tuning.

672 3.5.2 SmartPhantom 673

674 To study in real time the dose profile of Stage 2 beams, the SmartPhantom [Barber (2018)] is being
675 developed. This is a water-filled phantom, which is instrumented with planes of scintillating fibres, by
676 which to infer the dose distribution with distance. The detection elements of the SmartPhantom are 250 μm
677 diameter, round scintillating fibres. Each fibre station consist of two planes of fibres, in which the fibre
678 directions are orthogonal. Five fibre stations are arranged in the phantom in front of the cell-culture flask.
679 The fibres may be coupled to photodiodes, or a CMOS camera. Simulations in GEANT4 are being used to
680 develop analysis techniques by which to predict the position of the Bragg peak shot-by-shot. The beam
681 profile and dose delivered can then be calculated in real time. The key emphasis is to be able to derive these
682 parameters from shot-by-shot data, and not purely from simulations.

683 3.5.3 Beam line Instrumentation 684

685 The instrumentation requirement begins with the Ti:Sapphire laser. The laser focal spot will be characterised
686 using a camera-based system and high-speed wavefront measurements [Wang (2014)] from COTS vendors.

687 For the Stage 1 beam line, beam position monitors (BPMs) will be needed for beam steering. Because
688 of the low beam energy, non-intercepting BPMs using capacitive pickup buttons will be used. Custom
689 pickups will be needed to match the beam pipe geometry but COTS electronics are available. The beam
690 current will be monitored near the end of each beam line, using integrating current toroids (ICT), backed
691 up with the option of insertable multi-layer Faraday cups (MLFC) to give absolute beam current and energy
692 measurements. Beam profiles could be measured by SEM grids on both Stage 1 and Stage 2 beam lines.
693 For Stage 1, these monitors will be mounted on pneumatic actuators to avoid scattering. Each end station
694 could be equipped with insertable “pepper-pot” emittance monitors and a transverse deflection cavity with
695 fluorescent screen could be provided for bunch shape measurements.

696 The BPMs on the FFA will require pickup designs suitable for the unusual, wide and shallow, vacuum
697 vessel. The FFA at the KURNS facility in Kyoto is of a similar layout [Uesugi (2018)] and uses a kicker
698 and capacitive pickup to perform tune measurements in each transverse direction. A minimum of one BPM
699 every second cell will be used in the FFA so that the beam orbit can be measured. BPMs will also be

700 required close to the injection and extraction septa. The BPM system may be able to use COTS electronics,
701 but the pickups will be based on the KURNS design of multiple electrodes arranged across the vacuum
702 vessel width.

703 The DAQ needs to be able to store calibration data and apply corrections in real time. It is necessary to
704 be able to find the beam centre from a profile, even when the profile may be non-Gaussian and possibly
705 asymmetric. FPGAs can be used to perform fast fitting and pattern recognition of beam profiles. The
706 instrumentation will be integrated with the accelerator control system to be able to provide fast feedback
707 and adjustment of the beam parameters in real time.

708

709 **3.6 Biological end stations**

710 In order to deliver a successful radiobiological research programme, high-end and fully equipped *in vitro*
711 and *in vivo* end-stations will be housed within the LhARA facility. The two *in vitro* end-stations (high
712 and low energy) will contain vertically-delivered beam lines which will be used for the irradiation of 2D
713 monolayer and 3D-cell systems (spheroids and patient-derived organoids) in culture. The beam line within
714 the end-stations will be housed in sealed units that will be directly sourced with appropriate gases (carbon
715 dioxide and nitrogen), allowing for the cells within culture plates to be incubated for a short time in stable
716 conditions prior to and during irradiation. This will also enable the chamber to act, where necessary, as a
717 hypoxia unit (0.1%–5% oxygen concentration). Furthermore, these sealed units will contain robotics to
718 enable simple movement of the numerous cell culture plates housed within to be placed into and taken
719 away from the beam.

720 The *in vitro* end-stations will be located within a research laboratory equipped with up-to-date and
721 state-of-the-art facilities. This, coupled with two separate end-stations and multiple workspaces, will enable
722 multiple groups of researchers to perform productive and high-quality biological research. The laboratory
723 will include all the vital equipment for bench-top science, sample processing and analysis (e.g. refrigerated
724 centrifuges and light/fluorescent microscopes), along with the equipment required for contaminant-free cell
725 culture (e.g. humidified CO₂ cell culture incubators, Class II biological safety cabinets), and for the storage
726 of biological samples and specimens (e.g. –20°C and –80°C freezers and fridges). The laboratory will also
727 house an X-ray irradiator (allowing direct RBE comparisons between conventional photon irradiation, and
728 the proton and carbon ions delivered by the accelerator), hypoxia chamber (for long-term hypoxia studies),
729 a robotic workstation (handling and processing of large sample numbers, assisting in high-throughput
730 screening experiments), and an ultra-pure-water delivery system. These facilities will enable a myriad of
731 biological end-points to be investigated in both normal- and tumour-cell models not only from routine
732 clonogenic survival and growth assays, but will expand significantly on more complex end-points (e.g.
733 inflammation, angiogenesis, senescence and autophagy) as these experiments are difficult to perform at
734 current clinical research beams due to limited time and facilities.

735 The *in vivo* end-station will be served with high-energy proton and carbon ions capable of penetrating
736 deeper into tissues allowing the irradiation of whole animals. The ability to perform *in vivo* pre-clinical
737 studies is vital for the future effective translation of the research into human cancer patients where optimum
738 treatment strategies and reduction of side-effects can be defined. The *in vivo* end-station will allow the
739 irradiation of a number of small-animal models (e.g. xenograft mouse and rat models) which can further
740 promote an examination of particular ions on the appropriate biological end-points (e.g. tumour growth
741 and normal tissue responses). The end-station will contain a small-animal handling area which will allow
742 for the anaesthetisation of animals prior to irradiation. To enable the irradiation of small target volumes
743 with a high level of precision and accuracy, an image guidance system (e.g. computed tomography) will be

744 available. The animals will subsequently be placed in temperature-controlled holder tubes enabling the
745 correct positioning of the relevant irradiation area in front of the beam line. The beam size is sufficient to
746 give flexibility in the different irradiation conditions, in particular through passive scattering, pencil-beam
747 scanning, and micro-beam irradiation, to be investigated at both conventional and FLASH dose rates. It is
748 envisaged that the animals will be taken off-site post-irradiation to a nearby animal-holding facility for a
749 follow-up period where biological measurements will be conducted.

750

751 3.7 Infrastructure and integration

752 The LhARA facility will encompass two floors of roughly 42 m in length and 18 m wide. The ground floor
753 will contain the laser, accelerator, and *in vivo* end station while the first floor will house the laboratory area
754 and the two *in vitro* end stations. The entire facility will require radiation protection in the form of concrete
755 shielding, which will delineate the facility into three principal areas: a radiation-controlled access area, a
756 laser controlled access area, and a laboratory limited-access area.

757 It is envisaged that LhARA will be built at an STFC National Laboratory or equivalent research institute
758 which has an established safety-management system and culture in place. At STFC, a comprehensive set of
759 Safety Codes has been developed to cover the hazards associated with working in such an environment.
760 STFC Safety Codes applicable to LhARA include: risk management, construction, biological safety,
761 working with lasers, working with time-varying electro-magnetic fields, management of ionising radiation,
762 and electrical safety. In practice at STFC, these codes are backed-up by the knowledge, skills and experience
763 of staff, and by appointed responsible persons such as Radiation Protection Advisors, Laser Responsible
764 Officers, and Authorising Engineers. In addition, STFC operates many facilities that encompass the same
765 hazards as LhARA, which, for lasers, include the Gemini Target Areas 2 and 3 [STFC (2019a)] as well as
766 the new EPAC (Extreme Photonics Application Centre) [STFC (2019b)] and for accelerators include FETS
767 (Front End Test Stand) [Letchford et al. (2015)], and the ISIS Neutron and Muon Source [STFC (2019c)].
768 Safety systems and equipment will be required for LhARA, which will include Class II biological safety
769 cabinets for contaminant-free cell culture for *in vitro* radiobiological experiments.

770 For a facility such as LhARA, radiation safety is a primary concern and all work will be completed
771 under Regulation 8 of the Ionising Radiations Regulations 2017 (IRR17) [HSE (2018)], which requires a
772 radiation risk assessment before commencing a new work activity involving ionising radiation.

773 The infrastructure and integration of the LhARA facility will require R&D in four key areas: risk analysis
774 (project risks), risk assessments (safety risks), radiation simulations, and controls development. The risk
775 analysis will cover all aspects of the facility, such as funding and resource availability, not just technical
776 risks. A safety-risk assessment will be performed to describe and control all potential safety risks in the
777 facility. The safety-risk assessment will, to a reasonable degree, identify all pieces of equipment that
778 require safety mitigations and identify control measures that must be put in place. Coupled closely with the
779 safety-risk assessment, radiation simulations will be developed to characterise the radiation hazards in and
780 around the LhARA facility. The last area to require R&D will be the control systems. It is expected that the
781 facility will use the Experimental Physics and Industrial Control System (EPICS), which can be further
782 developed at this stage.

783

4 PERFORMANCE

784 The dose distributions delivered to the end stations were evaluated using BDSIM. Figure 11 shows the
785 energy lost by the beam as it enters the low-energy *in vitro* end station. The beam passes through the

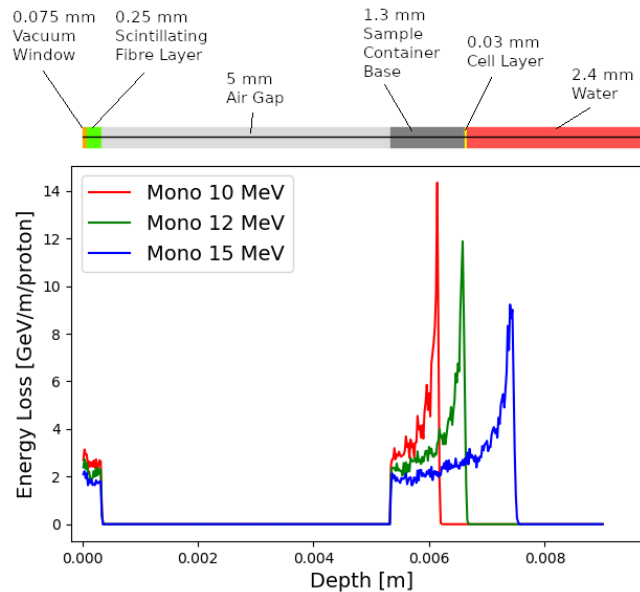


Figure 11. Energy loss as a function of depth in the low-energy *in vitro* end station for three monoenergetic proton energies: 10 MeV; 12 MeV; and 15 MeV. Each beam was simulated using 10^4 particles at the start of the simulated end station.

786 vacuum window, a layer of scintillating fibre, and a 5 mm air gap. The beam then enters the cell-sample
 787 container, assumed to be polystyrene, which supports a $30\ \mu\text{m}$ thick layer of cells, modelled using the
 788 Geant4 material “G4.SKIN_ICRP” [NIST (2017)]. The transverse momentum of protons in the beam was
 789 assumed to be Gaussian distributed, with a lateral spread small enough for the beam to be fully contained
 790 within the required spot size of 3 cm. Figure 11 shows that a proton beam with 10 MeV kinetic energy
 791 does not reach the cell. The Bragg peak of a 12 MeV proton beam is located close to the cell layer, while
 792 a 15 MeV beam, the maximum energy specified for delivery to the low-energy *in vitro* end station, has
 793 a Bragg peak located beyond the cell layer. LhARA’s ability to deliver various energies will allow the
 794 investigation of radiobiological effects for irradiations using different parts of the Bragg peak, effectively
 795 varying the LET across the sample.

796 The maximum dose that can be delivered was evaluated for a variety of beam energies. The dose was
 797 estimated from simulations by calculating the energy deposited in a volume of water corresponding in size
 798 to the sensitive volume of a PTW 23343 Markus ion chamber [PTW (2019/2020)] placed at the position
 799 of the Bragg peak in each case. The cylindrical chamber has a radius of 2.65 mm and a depth of 2 mm,
 800 giving a volume of about $4.4 \times 10^{-8}\ \text{m}^3$. The total energy deposited within the chamber was recorded and
 801 converted into dose in units of Gray.

802 For the low-energy *in vitro* end station the minimum spot size is specified to have a diameter of 10 mm,
 803 which is larger than the area of the chamber. A single shot of 10^9 protons at 12 MeV with the minimum
 804 design spot size deposits $3.1 \times 10^{-4}\ \text{J}$ in the chamber volume, corresponding to a dose of 7.1 Gy. For this
 805 simulation, the thickness of the sample container was reduced so that the Bragg peak could be positioned
 806 within the chamber volume. For the bunch length of 7.0 ns the maximum instantaneous dose rate is
 807 $1.0 \times 10^9\ \text{Gy/s}$ and the average dose rate is 71 Gy/s assuming a repetition rate of 10 Hz. A single shot of
 808 10^9 protons at 15 MeV deposits $5.6 \times 10^{-4}\ \text{J}$ in the chamber volume corresponding to a dose of 12.8 Gy.

Table 5. Summary of expected maximum dose per pulse and dose rates that LhARA can deliver for minimum beam sizes. These estimates are based on Monte Carlo simulations using a bunch length of 7 ns for 12 MeV and 15 MeV proton beams, 41.5 ns for the 127 MeV proton beam and 75.2 ns for the 33.4 MeV/u carbon beam. The average dose rate is based on the 10 Hz repetition rate of the laser source.

	12 MeV Protons	15 MeV Protons	127 MeV Protons	33.4 MeV/u Carbon
Dose per pulse	7.1 Gy	12.8 Gy	15.6 Gy	73.0 Gy
Instantaneous dose rate	1.0×10^9 Gy/s	1.8×10^9 Gy/s	3.8×10^8 Gy/s	9.7×10^8 Gy/s
Average dose rate	71 Gy/s	128 Gy/s	156 Gy/s	730 Gy/s

809 This gives an instantaneous dose rate of 1.8×10^9 Gy/s and an average dose rate of 128 Gy/s assuming the
810 same bunch length and repetition rate as for the 12 MeV case.

811 For the high-energy *in vitro* end station a different setup was used for high energy proton beams. A
812 similar design to the low-energy end station was used but with the air gap increased from 5 mm to 5 cm and
813 a water phantom was placed at the end of the air gap instead of a cell culture plate. The water phantom
814 used in the simulation was based upon the PTC T41023 water phantom [PTW (2009)]. In addition, the
815 smaller minimum design beam size of 1 mm was used. A single shot of 10^9 protons at 127 MeV deposits
816 6.9×10^{-4} J in the chamber at the pristine Bragg peak depth corresponding to a dose of 15.6 Gy, an
817 instantaneous dose rate of 3.8×10^8 Gy/s and an average dose rate of 156 Gy/s. The end-station design
818 assumed for a 33.4 MeV/u carbon beam was the same as that used for the low-energy *in vitro* end station
819 due to the limited range in water of the carbon beam. The intensity of the beam is a factor of 12 less than
820 for protons in order to preserve the same strength of the space-charge effect at injection into the FFA with
821 the same beam parameters, as the incoherent space charge tune shift is proportional to q^2/A and inversely
822 proportional to $\beta^2\gamma^3$, where q corresponds to the particle charge, A its mass number and β , γ its relativistic
823 parameters. A single pulse of 8.3×10^7 ions, deposits 3.2×10^{-3} J at the depth of the pristine Bragg peak,
824 leading to an instantaneous dose rate of 9.7×10^8 Gy/s and a maximum average dose rate of 730 Gy/s.

825 The expected maximum dose rates are summarised in table 5. The instantaneous dose rates depend on
826 the bunch length which differs depending on the energies. For the low-energy *in vitro* line a 7 ns bunch
827 length is assumed here for all energies. While for the higher energies, a 127 MeV proton beam is delivered
828 with a bunch length of 41.5 ns, and a bunch length of 75.2 ns for a 33.4 MeV/u carbon beam. The same
829 repetition rate of 10 Hz was used for all energies. The minimum beam size at the start of the end station for
830 the 12 MeV and 15 MeV proton-beam simulations was 1 cm. A 1 mm beam size was used for the 127 MeV
831 proton beam and 33.4 MeV/u carbon-ion beam simulations.

832

5 CONCLUSIONS

833 The initial conceptual design of LhARA, the Laser-hybrid Accelerator for Radiobiological Applications,
834 has been described and its performance evaluated in simulations that take into account the key features of
835 the facility. LhARA combines a laser-driven source to create a large flux of protons or light ions which are
836 captured and formed into a beam by strong-focusing plasma lenses thus evading the current space-charge
837 limit on the instantaneous dose rate that can be delivered. Acceleration, performed using an FFA, preserves
838 the unique flexibility in the time, spectral, and spatial structure of the beam afforded by the laser-driven
839 source. The ability to trigger the laser pulse that initiates the production of protons or ions at LhARA will
840 allow the time structure of the beam to be varied to interrupt the chemical and biological pathways that

841 determine the biological response to ionising radiation. In addition, the almost parallel beam that LhARA
842 will deliver can be varied to illuminate a circular area with a maximum diameter of between 1 cm and 3 cm
843 with an almost uniform dose or focused to a spot with diameter of ~ 1 mm. These features make LhARA
844 the ideally flexible tool for the systematic study of the radiobiology of proton and ion beams.

845 The technologies demonstrated in LhARA have the potential to be developed to make “best in class”
846 treatments available to the many by reducing the footprint of future particle-beam therapy systems. The
847 laser-hybrid approach, therefore, will allow radiobiological studies and eventually radiotherapy to be
848 carried out in completely new regimes, delivering a variety of ion species in a broad range of time structures
849 and spatial configurations at instantaneous dose rates up to and potentially significantly beyond the current
850 ultra-high dose-rate “FLASH” regime.

851 LhARA has the potential to drive a change in clinical practice in the medium term by increasing the
852 wealth of radiobiological knowledge. This enhanced understanding in turn may be used to devise new
853 approaches to decrease radio-toxicity on normal tissue while maintaining, or even enhancing, the tumour-
854 kill probability. The radiobiology programme in combination with the demonstration in operation of the
855 laser-hybrid technique means that the execution of the LhARA programme has the potential to drive a
856 step-change in the clinical practice of proton- and ion-beam therapy.

857

ACKNOWLEDGEMENTS

858 The work described here was made possible by a grant from the Science and Technology Facilities Council
859 (ST/T002638/1). Additional support was provided by the STFC Rutherford Appleton and Daresbury
860 Laboratories and members of the LhARA consortium. We gratefully acknowledge all sources of support.
861 A pre-publication review of the pre-CDR for LhARA was carried out by P. Bolton (LMU, Munich),
862 M. Lamont (CERN), Y. Prezado (Institut Curie), and F. Romano (INFN-LNS and the National Physical
863 Laboratory). We are grateful to the review panel for their support and detailed feedback on the draft
864 pre-CDR.

865

REFERENCES

- 866 (2009). *User Manual Water Phantom T41023*. PTW-Freiburg Physikalisch-Technische Werkstätten Dr.
867 Pchlau GmbH, d738.131.00/02 en edn.
- 868 (2019/2020). *Ionizing Radiation Detectors*. PTW-Freiburg Physikalisch-Technische Werkstätten Dr.
869 Pchlau GmbH
- 870 [Dataset] (2020). Vsim for plasma. <https://www.txcorp.com/vsim>
- 871 [Dataset] A-SAIL Project (2020). A-sail project. [https://www.qub.ac.uk/
872 research-centres/A-SAILProject/](https://www.qub.ac.uk/research-centres/A-SAILProject/)
- 873 Amin, T., Barlow, R., Ghithan, S., Royb, G., and Schuhb, S. (2018). Formation of a uniform ion beam
874 using octupole magnets for bioleir facility at cern. *JINST* 13, P04016
- 875 Atun, R., Jaffray, D. A., Barton, M. B., Bray, F., Baumann, M., Vikram, B., et al. (2015). Expanding
876 global access to radiotherapy. *The Lancet Oncology* 16, 1153 – 1186. doi:[https://doi.org/10.1016/
877 S1470-2045\(15\)00222-3](https://doi.org/10.1016/S1470-2045(15)00222-3)
- 878 Aurand, B., Grieser, S., Toncian, T., Aktan, E., Cerchez, M., Lessmann, L., et al. (2019). A multihertz,
879 kiloelectronvolt pulsed proton source from a laser irradiated continuous hydrogen cluster target. *Physics
880 of Plasmas* 26, 073102. doi:10.1063/1.5093287

- 881 Autin, B., Carli, C., D'Amico, T., Gröbner, O., Martini, M., and Wildner, E. (1998). *BeamOptics:*
882 *A program for analytical beam optics*. Tech. Rep. CERN-98-06, European Organization for
883 Nuclear Research (CERN). [http://inis.iaea.org/search/search.aspx?orig_q=RN:](http://inis.iaea.org/search/search.aspx?orig_q=RN:30052986)
884 30052986
- 885 Barber, G. (2018). Outline design and cost estimate for the SmartPhantom. *Unpublished note*
- 886 Bin, J., Allinger, K., Assmann, W., Dollinger, G., Drexler, G. A., Friedl, A. A., et al. (2012). A laser-
887 driven nanosecond proton source for radiobiological studies. *Applied Physics Letters* 101, 243701.
888 doi:10.1063/1.4769372
- 889 Bin, J., Ma, W., Wang, H., Streeter, M., Kreuzer, C., Kiefer, D., et al. (2015). Ion Acceleration Using
890 Relativistic Pulse Shaping in Near-Critical-Density Plasmas. *Physical Review Letters* 115, 064801.
891 doi:10.1103/PhysRevLett.115.064801
- 892 Bray, F., Ferlay, J., Soerjomataram, I., Siegel, R. L., Torre, L. A., and Jemal, A. (2018). Global cancer
893 statistics 2018: GLOBOCAN estimates of incidence and mortality worldwide for 36 cancers in 185
894 countries. *CA: A Cancer Journal for Clinicians* 68, 394–424. doi:10.3322/caac.21492
- 895 Bulanov, S., Esirkepov, T., Khoroshkov, V., Kuznetsov, A., and Pegoraro, F. (2002). Oncological
896 hadrontherapy with laser ion accelerators. *Physics Letters A* 299, 240–247. doi:https://doi.org/10.1016/
897 S0375-9601(02)00521-2
- 898 Carter, R. J., Nickson, C. M., Thompson, J. M., Kacperek, A., Hill, M. A., and Parsons, J. L. (2018).
899 Complex dna damage induced by high linear energy transfer alpha-particles and protons triggers a
900 specific cellular dna damage response. *International Journal of Radiation Oncology*Biophysics*Physics*
901 100, 776 – 784. doi:https://doi.org/10.1016/j.ijrobp.2017.11.012
- 902 Chaudhary, P., Gwynne, D., Doria, D., Romagnani, L., Maiorino, C., Padua, H., et al. (2017). Effectiveness
903 of laser accelerated ultra high dose rate protons in DNA DSB damage induction under hypoxic conditions.
904 In *44th EPS Conference on Plasma Physics, EPS 2017* (European Physical Society (EPS)), vol. 44F.
905 P1.217
- 906 Chaudhary, P., Marshall, T. I., Perozziello, F. M., Manti, L., Currell, F. J., Hanton, F., et al. (2014). Relative
907 Biological Effectiveness Variation Along Monoenergetic and Modulated Bragg Peaks of a 62-MeV
908 Therapeutic Proton Beam: A Preclinical Assessment. *International Journal of Radiation Oncology •*
909 *Biology • Physics* 90, 27–35. doi:10.1016/j.ijrobp.2014.05.010
- 910 Chen, S. N., Vranic, M., Gangolf, T., Boella, E., Antici, P., Bailly-Grandvaux, M., et al. (2017). Collimated
911 protons accelerated from an overdense gas jet irradiated by a 1 μm wavelength high-intensity short-pulse
912 laser. *Scientific Reports* 7, 13505. doi:10.1038/s41598-017-12910-6
- 913 Cirrone, G. A. P., Margarone, D., Maggiore, M., Anzalone, A., Borghesi, M., Jia, S. B., et al. (2013).
914 ELIMED: a new hadron therapy concept based on laser driven ion beams. In *Laser Acceleration of*
915 *Electrons, Protons, and Ions II; and Medical Applications of Laser-Generated Beams of Particles II;*
916 *and Harnessing Relativistic Plasma Waves III*, eds. E. Esarey, C. B. Schroeder, W. P. Leemans, K. W. D.
917 Ledingham, and D. A. Jaroszynski. International Society for Optics and Photonics (SPIE), vol. 8779,
918 216 – 225. doi:10.1117/12.2026530
- 919 Clark, E. L., Krushelnick, K., Davies, J. R., Zepf, M., Tatarakis, M., Beg, F. N., et al. (2000). Measurements
920 of energetic proton transport through magnetized plasma from intense laser interactions with solids.
921 *Phys. Rev. Lett.* 84, 670–673. doi:10.1103/PhysRevLett.84.670
- 922 Daido, H., Nishiuchi, M., and Pirozhkov, A. S. (2012). Review of laser-driven ion sources and their
923 applications. *Reports on Progress in Physics* 75, 56401. doi:10.1088/0034-4885/75/5/056401
- 924 Dann, S. J. D., Baird, C. D., Bourgeois, N., Chekhlov, O., Eardley, S., Gregory, C. D., et al. (2019).
925 Laser wakefield acceleration with active feedback at 5 Hz. *Phys. Rev. Accel. Beams* 22, 041303.

- 926 doi:10.1103/PhysRevAccelBeams.22.041303
- 927 Datta, N. R., Rogers, S., and Bodis, S. (2019). Challenges and Opportunities to Realize “The 2030 Agenda
928 for Sustainable Development” by the United Nations: Implications for Radiation Therapy Infrastructure
929 in Low- and Middle-Income Countries. *International Journal of Radiation Oncology*Biophysics*
930 105, 918–933. doi:<https://doi.org/10.1016/j.ijrobp.2019.04.033>
- 931 De Loos, M. J. and Van der Geer, S. B. (1996). General Particle Tracer: A New 3D Code for Accelerator
932 and Beamline Design
- 933 deGrassie, J. S. and Malmberg, J. H. (1980). Waves and transport in the pure electron plasma. *The Physics*
934 *of Fluids* 23, 63–81. doi:10.1063/1.862864
- 935 Doria, D., Kakolee, K. F., Kar, S., Litt, S. K., Fiorini, F., Ahmed, H., et al. (2012). Biological effectiveness
936 on live cells of laser driven protons at dose rates exceeding 10^9 Gy/s. *AIP Advances* 2, 011209.
937 doi:10.1063/1.3699063
- 938 Favaudon, V., Caplier, L., Monceau, V., Pouzoulet, F., Sayarath, M., Fouillade, C., et al. (2014). Ultrahigh
939 dose-rate flash irradiation increases the differential response between normal and tumor tissue in mice.
940 *Science Translational Medicine* 6, 245ra93–245ra93. doi:10.1126/scitranslmed.3008973
- 941 Fiorini, F., Kirby, D., Borghesi, M., Doria, D., Jeynes, J. C., Kakolee, K. F., et al. (2011). Dosimetry and
942 spectral analysis of a radiobiological experiment using laser-driven proton beams. *Phys Med Biol* 56,
943 6969–6982
- 944 Fitzmaurice, C., Akinyemiju, T. F., Al Lami, F. H., Alam, T., Alizadeh-Navaei, R., Allen, C., et al. (2018).
945 Global, Regional, and National Cancer Incidence, Mortality, Years of Life Lost, Years Lived With
946 Disability, and Disability-Adjusted Life-Years for 29 Cancer Groups, 1990 to 2016. *JAMA Oncology* 4,
947 1553. doi:10.1001/jamaoncol.2018.2706
- 948 Fourkal, E., Li, J. S., Ding, M., Tajima, T., and Ma, C. M. (2003). Particle selection for laser-accelerated
949 proton therapy feasibility study. *Medical Physics* 30, 1660–1670. doi:10.1118/1.1586268
- 950 Fourier, J., Martinache, F., Meot, F., and Pasternak, J. (2008). Spiral ftag lattice design tools. application
951 to 6-d tracking in a proton-therapy class lattice. *Nucl. Instrum. Meth. A* 589, 133–142. doi:10.1016/j.
952 nima.2008.01.082
- 953 Gabor, D. (1947). A Space-Charge Lens for the Focusing of Ion Beams. *Nature* 160, 89–90. doi:10.1038/
954 160089b0
- 955 Gauthier, M., Curry, C. B., Göde, S., Brack, F.-E., Kim, J. B., MacDonald, M. J., et al. (2017). High
956 repetition rate, multi-mev proton source from cryogenic hydrogen jets. *Applied Physics Letters* 111,
957 114102. doi:10.1063/1.4990487
- 958 Giovannini, G., Böhlen, T., Cabal, G., Bauer, J., Tessonnier, T., Frey, K., et al. (2016). Variable RBE in
959 proton therapy: comparison of different model predictions and their influence on clinical-like scenarios.
960 *Radiation Oncology* 11, 68. doi:10.1186/s13014-016-0642-6
- 961 Grote, H. and Schmidt, F. (2003). MAD-X: An upgrade from MAD8. *Conf. Proc. C* 030512, 3497
- 962 HSE (2018). *Work with ionising radiation - Ionising Radiations Regulations 2017* (Crown)
- 963 IBA (2019). Flash irradiation delivered in a clinical treatment room [https://iba-worldwide.com/
964 content/pt/proton-flash-irradiation-delivered-clinical-treatment-room](https://iba-worldwide.com/content/pt/proton-flash-irradiation-delivered-clinical-treatment-room)
- 965
- 966 Jones, B., McMahon, S. J., and Prise, K. M. (2018). The Radiobiology of Proton Therapy: Challenges and
967 Opportunities Around Relative Biological Effectiveness. *Clinical Oncology* 30, 285–292. doi:10.1016/j.
968 clon.2018.01.010.
- 969 Karger, C. P. and Peschke, P. (2017). RBE and related modeling in carbon-ion therapy. *Physics in Medicine*
970 *& Biology* 63, 01TR02. doi:10.1088/1361-6560/aa9102

- 971 [Dataset] Kirschner, J., Mutný, M., Hiller, N., Ischebeck, R., and Krause, A. (2019). Adaptive and safe
972 bayesian optimization in high dimensions via one-dimensional subspaces
- 973 Kraft, S. D., Richter, C., Zeil, K., Baumann, M., Beyreuther, E., Bock, S., et al. (2010). Dose-dependent
974 biological damage of tumour cells by laser-accelerated proton beams. *New Journal of Physics* 12, 85003.
975 doi:10.1088/1367-2630/12/8/085003
- 976 Krest, D., Laslett, L., Jones, L. W., Symon, K., and Terwilliger, K. (1956). *Fixed field alternating gradient*
977 *particle accelerators*. Tech. Rep. MURA-109, MURA-DWK-KRS-LJL-LWJ-KMT-3, Midwestern
978 Universities Research Association (MURA)
- 979 Kurup, A. (2019). Diagnostics for LhARA. *Low energy ion beam diagnostics workshop, Imperial College*
980 Lagrange, J. B., Appleby, R. B., Garland, J. M., Pasternak, J., and Tygier, S. (2018). Racetrack FFAG
981 muon decay ring for nuSTORM with triplet focusing. *JINST* 13, P09013. doi:10.1088/1748-0221/13/
982 09/P09013
- 983 Letchford, A. et al. (2015). Status of the ral front end test stand. In *IPAC*
- 984 Loeffler, J. S. and Durante, M. (2013). Charged particle therapy—optimization, challenges and future
985 directions. *Nature Reviews Clinical Oncology* 10, 411–424. doi:10.1038/nrclinonc.2013.79
- 986 Lühr, A., von Neubeck, C., Krause, M., and Troost, E. G. C. (2018). Relative biological effectiveness in
987 proton beam therapy – Current knowledge and future challenges. *Clinical and Translational Radiation*
988 *Oncology* 9, 35–41. doi:10.1016/j.ctro.2018.01.006
- 989 Malka, V., Fritzler, S., Lefebvre, E., d’Humières, E., Ferrand, R., Grillon, G., et al. (2004). Practicability of
990 proton therapy using compact laser systems. *Medical Physics* 31, 1587–1592. doi:10.1118/1.1747751
- 991 Malmberg, J. H., Driscoll, C. F., Beck, B., Eggleston, D. L., Fajans, J., Fine, K., et al. (1988). Experiments
992 with pure electron plasmas. *AIP Conference Proceedings* 175, 28–74. doi:10.1063/1.37613
- 993 Manti, L., Perozziello, F. M., Borghesi, M., Candiano, G., Chaudhary, P., Cirrone, G. A., et al. (2017).
994 The radiobiology of laser-driven particle beams: Focus on sub-lethal responses of normal human cells.
995 *Journal of Instrumentation* 12. doi:10.1088/1748-0221/12/03/C03084
- 996 Margarone, D., Cirrone, G. A. P., Cuttone, G., Amico, A., Andò, L., Borghesi, M., et al. (2018).
997 Elimaia: A laser-driven ion accelerator for multidisciplinary applications. *Quantum Beam Science* 2.
998 doi:10.3390/qubs2020008
- 999 Margarone, D., Velyhan, A., Dostal, J., Ullschmied, J., Perin, J. P., Chatain, D., et al. (2016). Proton
1000 acceleration driven by a nanosecond laser from a cryogenic thin solid-hydrogen ribbon. *Phys. Rev. X* 6,
1001 041030. doi:10.1103/PhysRevX.6.041030
- 1002 Masood, U., Bussmann, M., Cowan, T. E., Enghardt, W., Karsch, L., Kroll, F., et al. (2014). A
1003 compact solution for ion beam therapy with laser accelerated protons. *Applied Physics B* 117, 41–52.
1004 doi:https://doi.org/10.1007/s00340-014-5796-z
- 1005 Masood, U., Cowan, T. E., Enghardt, W., Hofmann, K. M., Karsch, L., Kroll, F., et al. (2017). A
1006 light-weight compact proton gantry design with a novel dose delivery system for broad-energetic
1007 laser-accelerated beams. *Physics in Medicine & Biology* 62, 5531–5555. doi:10.1088/1361-6560/aa7124
- 1008 Meusel, O., Droba, M., Glaeser, B., and Schulte, K. (2013). Experimental studies of stable confined electron
1009 clouds using Gabor lenses. *Conf. Proc. C* 1206051, 157–160. doi:10.5170/CERN-2013-002.157
- 1010 Morrison, J. T., Feister, S., Frische, K. D., Austin, D. R., Ngirmang, G. K., Murphy, N. R., et al. (2018).
1011 MeV proton acceleration at kHz repetition rate from ultra-intense laser liquid interaction. *New Journal*
1012 *of Physics* 20, 22001. doi:10.1088/1367-2630/aaa8d1
- 1013 Nevay, L. J. et al. (2020). Bdsim: An accelerator tracking code with particle-matter interactions. *Computer*
1014 *Physics Communications* , 107200

- 1015 NIST (2017). *NIST Standard Reference Database 124* (National Institute of Standards and Technology).
1016 doi:<https://dx.doi.org/10.18434/T4NC7P>
- 1017 Noaman-ul Haq, M., Ahmed, H., Sokollik, T., Yu, L., Liu, Z., Yuan, X., et al. (2017). Statistical analysis of
1018 laser driven protons using a high-repetition-rate tape drive target system. *Phys. Rev. Accel. Beams* 20,
1019 041301. doi:10.1103/PhysRevAccelBeams.20.041301
- 1020 Obst, L., Göde, S., Rehwald, M., Brack, F.-E., Branco, J., Bock, S., et al. (2017). Efficient laser-driven
1021 proton acceleration from cylindrical and planar cryogenic hydrogen jets. *Scientific Reports* 7, 10248.
1022 doi:10.1038/s41598-017-10589-3
- 1023 Paganetti, H. (2014). Relative biological effectiveness (RBE) values for proton beam therapy. Variations as
1024 a function of biological endpoint, dose, and linear energy transfer. *Phys. Med. Biol.* 59, R419
- 1025 Paganetti, H. and van Luijk, P. (2013). Biological considerations when comparing proton therapy with
1026 photon therapy. *Seminars in Radiation Oncology* 23, 77 – 87. doi:[https://doi.org/10.1016/j.semradonc.](https://doi.org/10.1016/j.semradonc.2012.11.002)
1027 2012.11.002. Controversies in Proton Therapy
- 1028 Planche, T., Fourier, J., Lancelot, J. L., Meot, F., Neuveglise, D., and Pasternak, J. (2009). Design of a
1029 prototype gap shaping spiral dipole for a variable energy protontherapy FFAG. *Nucl. Instrum. Meth.*
1030 A604, 435–442. doi:10.1016/j.nima.2009.02.026
- 1031 Pommarel, L., Vauzour, B., Mégnin-Chanet, F., Bayart, E., Delmas, O., Goudjil, F., et al. (2017). Spectral
1032 and spatial shaping of a laser-produced ion beam for radiation-biology experiments. *Physical Review*
1033 *Accelerators and Beams* 20, 1–10. doi:10.1103/PhysRevAccelBeams.20.032801
- 1034 Pozimski, J. and Aslaninejad, M. (2013). Gabor lenses for capture and energy selection of laser driven ion
1035 beams in cancer treatment. *Laser and Particle Beams* 31, 723—733. doi:10.1017/S0263034613000761
- 1036 Prezado, Y., Jouvion, G., Hardy, D., Patriarca, A., Nauraye, C., Bergs, J., et al. (2017). Proton minibeam
1037 radiation therapy spares normal rat brain: Long-Term Clinical, Radiological and Histopathological
1038 Analysis. *Scientific Reports* 7, 14403. doi:10.1038/s41598-017-14786-y
- 1039 [Dataset] PTCOG (2020). Particle Therapy Co-Operative Group. [https://www.ptcog.ch/index.](https://www.ptcog.ch/index.php/patient-statistics)
1040 [php/patient-statistics](https://www.ptcog.ch/index.php/patient-statistics)
- 1041 Reiser, M. (1989). Comparison of gabor lens, gas focusing, and electrostatic quadrupole focusing for
1042 low-energy ion beams. In *Proceedings of the 1989 IEEE Particle Accelerator Conference, . 'Accelerator*
1043 *Science and Technology*. 1744–1747 vol.3
- 1044 Romano, F., Schillaci, F., Cirrone, G., Cuttone, G., Scuderi, V., Allegra, L., et al. (2016). The elimed
1045 transport and dosimetry beamline for laser-driven ion beams. *Nuclear Instruments and Methods in*
1046 *Physics Research Section A: Accelerators, Spectrometers, Detectors and Associated Equipment* 829,
1047 153–158. doi:<https://doi.org/10.1016/j.nima.2016.01.064>. 2nd European Advanced Accelerator Concepts
1048 Workshop – EAAC 2015
- 1049 Snavely, R. A., Key, M. H., Hatchett, S. P., Cowan, T. E., Roth, M., Phillips, T. W., et al. (2000). Intense
1050 high-energy proton beams from petawatt-laser irradiation of solids. *Phys. Rev. Lett.* 85, 2945–2948.
1051 doi:10.1103/PhysRevLett.85.2945
- 1052 [Dataset] STFC (2019a). The astra gemini facility. [https://www.clf.stfc.ac.uk/Pages/](https://www.clf.stfc.ac.uk/Pages/The-Astra-Gemini-Facility.aspx)
1053 [The-Astra-Gemini-Facility.aspx](https://www.clf.stfc.ac.uk/Pages/The-Astra-Gemini-Facility.aspx)
- 1054 [Dataset] STFC (2019b). Introducing the extreme photonics applications centre. [https://www.clf.](https://www.clf.stfc.ac.uk/Pages/EPAC-introduction-page.aspx)
1055 [stfc.ac.uk/Pages/EPAC-introduction-page.aspx](https://www.clf.stfc.ac.uk/Pages/EPAC-introduction-page.aspx)
- 1056 [Dataset] STFC (2019c). Isis neutron and muon source. [https://stfc.ukri.org/research/](https://stfc.ukri.org/research/our-science-facilities/isis-neutron-and-muon-source/)
1057 [our-science-facilities/isis-neutron-and-muon-source/](https://stfc.ukri.org/research/our-science-facilities/isis-neutron-and-muon-source/)
- 1058 Streeter, M. J. V., Dann, S. J. D., Scott, J. D. E., Baird, C. D., Murphy, C. D., Eardley, S., et al. (2018).
1059 Temporal feedback control of high-intensity laser pulses to optimize ultrafast heating of atomic clusters.

- 1060 *Applied Physics Letters* 112, 244101. doi:10.1063/1.5027297
- 1061 Symon, K. R., Kerst, D. W., Jones, L. W., Laslett, L. J., and Terwilliger, K. M. (1956). Fixed-field
1062 alternating-gradient particle accelerators. *Phys. Rev.* 103, 1837–1859. doi:10.1103/PhysRev.103.1837
- 1063 Systems, V. M. (2020). Flashforward consortium [https://www.varian.com/about-varian/
1064 research/flashforward-consortium](https://www.varian.com/about-varian/research/flashforward-consortium)
- 1065 Tanigaki, M., Mori, Y., Inoue, M., Mishima, K., Shiroya, S., Ishi, Y., et al. (2006). Present status of the
1066 ftag accelerators in kurri for ads study. In *EPAC 2006 - Contributions to the Proceedings*
- 1067 The LhARA consortium (2020). *The Laser-hybrid Accelerator for Radiobiological Applications*.
1068 Tech. Rep. CCAP-TN-01. [https://ccap.hep.ph.ic.ac.uk/trac/raw-attachment/
1069 wiki/Research/DesignStudy/PreCDR/Review/2020-03-31-LhARA_pre_CDR-d2.
1070 0.pdf](https://ccap.hep.ph.ic.ac.uk/trac/raw-attachment/wiki/Research/DesignStudy/PreCDR/Review/2020-03-31-LhARA_pre_CDR-d2.0.pdf)
- 1071 [Dataset] The World Health Organisation (2020). Cancer. [https://www.who.int/news-room/
1072 fact-sheets/detail/cancer](https://www.who.int/news-room/fact-sheets/detail/cancer)
- 1073 Thompson, R. C. (2015). PENNING TRAPS. In *Trapped Charged Particles (WORLD SCIENTIFIC
1074 (EUROPE))*, Advanced Textbooks in Physics. 1–33. doi:doi:10.1142/9781786340139_0001
- 1075 Tsoupas, N. et al. (1991). Uniform beam distributions using octupoles. *Proceedings of PAC 1991* ,
1076 1695–1697
- 1077 Uesugi, T. (2018). Betatron Tune Measurement . *FFA School, Osaka*
- 1078 Urakabe, E. et al. (1999). Beam-profile control using an octupole magnet. *Jpn. J. Appl. Phys.* 38,
1079 6145–6149
- 1080 Vitti, E. T. and Parsons, J. L. (2019). The radiobiological effects of proton beam therapy: Impact on dna
1081 damage and repair. *Cancers* 11. doi:10.3390/cancers11070946
- 1082 Vozenin, M. C., De Fornel, P., Petersson, K., Favaudon, V., Jaccard, M., Germond, J. F., et al. (2019). The
1083 Advantage of FLASH Radiotherapy Confirmed in Mini-pig and Cat-cancer Patients. *Clin. Cancer Res.*
1084 25, 35–42. doi:10.1158/1078-0432
- 1085 Wang, H. (2014). Wavefront measurement techniques used in high power lasers. *High Power Laser Science
1086 and Engineering* 2
- 1087 Wiggins, S. M., Boyd, M., Brunetti, E., Butler, N. M. H., Feehan, J. S., Gray, R. J., et al. (2019). Application
1088 programmes at the Scottish Centre for the Application of Plasma-based Accelerators (SCAPA). In
1089 *Relativistic Plasma Waves and Particle Beams as Coherent and Incoherent Radiation Sources III*, eds.
1090 D. A. Jaroszynski and M. Hur. International Society for Optics and Photonics (SPIE), vol. 11036, 93 –
1091 103. doi:10.1117/12.2520717
- 1092 Wilkens, J. J. and Oelfke, U. (2004). A phenomenological model for the relative biological effectiveness in
1093 therapeutic proton beams. *Physics in Medicine and Biology* 49, 2811–2825. doi:10.1088/0031-9155/49/
1094 13/004
- 1095 Willingale, L., Nagel, S. R., Thomas, A. G. R., Bellei, C., Clarke, R. J., Dangor, A. E., et al. (2009).
1096 Characterization of High-Intensity Laser Propagation in the Relativistic Transparent Regime through
1097 Measurements of Energetic Proton Beams. *Physical Review Letters* 102, 125002. doi:10.1103/
1098 PhysRevLett.102.125002
- 1099 Yogo, A., Maeda, T., Hori, T., Sakaki, H., Ogura, K., Nishiuchi, M., et al. (2011). Measurement of relative
1100 biological effectiveness of protons in human cancer cells using a laser-driven quasimonoenergetic proton
1101 beamline. *Applied Physics Letters* 98, 053701. doi:10.1063/1.3551623
- 1102 Yonemura, Y., Arima, H., Ikeda, N., Ishibashi, K., Maehata, K., Noro, T., et al. (2008). Status of center
1103 for accelerator and beam applied science of kyushu university. *EPAC 2008 - Contributions to the
1104 Proceedings*

- 1105 Zeil, K., Baumann, M., Beyreuther, E., Burris-Mog, T., Cowan, T. E., Enghardt, W., et al. (2013).
1106 Dose-controlled irradiation of cancer cells with laser-accelerated proton pulses. *Applied Physics B* 110,
1107 437–444. doi:10.1007/s00340-012-5275-3
- 1108 Zlobinskaya, O., Siebenwirth, C., Greubel, C., Hable, V., Hertenberger, R., Humble, N., et al. (2014).
1109 The effects of ultra-high dose rate proton irradiation on growth delay in the treatment of human tumor
1110 xenografts in nude mice. *Radiation Research* 181, 177–183. doi:10.1667/RR13464.1